



**University of Dundee**

## **Biophysical study of resin acid effects on phospholipid membrane 1 structure and properties**

Jagalski, Vivian; Barker, Robert; Topgaard, Daniel; Günther Pomorski, Thomas; Hamberger, Björn; Cárdenas, Marité

*Published in:*  
Biochimica et Biophysica Acta - Biomembranes

*DOI:*  
[10.1016/j.bbamem.2016.08.008](https://doi.org/10.1016/j.bbamem.2016.08.008)

*Publication date:*  
2016

*Document Version*  
Peer reviewed version

[Link to publication in Discovery Research Portal](#)

*Citation for published version (APA):*  
Jagalski, V., Barker, R., Topgaard, D., Günther Pomorski, T., Hamberger, B., & Cárdenas, M. (2016). Biophysical study of resin acid effects on phospholipid membrane 1 structure and properties. *Biochimica et Biophysica Acta - Biomembranes*, 1858(11), 2827-2838. DOI: 10.1016/j.bbamem.2016.08.008

### **General rights**

Copyright and moral rights for the publications made accessible in Discovery Research Portal are retained by the authors and/or other copyright owners and it is a condition of accessing publications that users recognise and abide by the legal requirements associated with these rights.

- Users may download and print one copy of any publication from Discovery Research Portal for the purpose of private study or research.
- You may not further distribute the material or use it for any profit-making activity or commercial gain.
- You may freely distribute the URL identifying the publication in the public portal.

### **Take down policy**

If you believe that this document breaches copyright please contact us providing details, and we will remove access to the work immediately and investigate your claim.

# 1 **Biophysical study of resin acid effects on phospholipid membrane structure and properties**

2  
3 Vivien Jagalski<sup>1</sup>, Robert Barker<sup>2</sup>, Daniel Topgaard<sup>3</sup>, Thomas Günther Pomorski<sup>4</sup>, Björn  
4 Hamberger<sup>4</sup>, Marité Cárdenas<sup>5,1</sup>

5 <sup>1</sup> *Nano Science Center and Department of Chemistry, University of Copenhagen, Copenhagen,*  
6 *Denmark.*

7 <sup>2</sup> *Institute Laue Langevin, 71 avenue de Matyrs, CS 20156, 38042 Grenoble Cedex 9, France.*  
8 *Current address: School of Science and Engineering, University of Dundee, Dundee DD1 4HN,*  
9 *United Kingdom.*

10 <sup>3</sup> *Division of Physical Chemistry, Chemistry Department, Lund University, Sweden*

11 <sup>4</sup> *Department of Plant and Environmental Sciences, University of Copenhagen, Copenhagen,*  
12 *Denmark.*

13 <sup>5</sup> *Biofilm – Research center for Biointerfaces and Department of Biomedical Science, Malmö*  
14 *University, Malmö, Sweden.*

## 16 **Abstract**

17 Hydrophobic resin acids (RAs) are synthesized by trees as part of their defence mechanisms. One of  
18 the functions of RAs in plant defence is suggested to be the perturbation of the cellular membrane.  
19 However, there is vast diversity of chemical structure within this class of molecules, and there are  
20 no clear correlations to the molecular mechanisms behind the RA's toxicity. In this study we  
21 unravel the molecular interactions of three closely related RAs dehydroabietic acid, neoabietic acid,  
22 and the synthetic analogue dichlorodehydroabietic acid with dipalmitoylphosphatidylcholine  
23 (DPPC) model membranes and the polar lipid extract of soybeans. The complementarity of the  
24 biophysical techniques used (PT ssNMR, DLS, NR, DSC, Cryo-TEM) allowed correlating changes  
25 at the vesicle level with changes at the molecular level and the co-localization of RAs within DPPC  
26 monolayer. Effects on DPPC membranes are correlated with the physical chemical properties of the  
27 RA and their toxicity.

## 29 **1. Introduction**

30 Resin acids (RAs) belong to an important class of natural biologically active compounds that form  
31 part of the defence mechanisms of certain plants, e.g. conifer trees [1]. Today they are widely  
32 applied as natural insecticides and have potential use in new industrial applications due to their  
33 antimicrobial and antifungal properties [2].

34

35 RAs are tricyclic diterpenes of the labdane type, which derive from the precursor geranylgeranyl  
36 diphosphate (GGPP), consist of 20 carbon atoms and carry a carboxyl group. Their high chemical  
37 diversity arises from various functional groups, diastereoisomers and the number and position of  
38 double bonds [1]. In order to circumvent toxic effects, the synthesis of natural RAs, e.g. in pines,  
39 takes place in specialized epithelial cells after which they are concentrated and stored in cell free  
40 resin ducts [3]. Additionally, a wide range of synthetic and modified RAs exist today, such as  
41 dichlorodehydroabietic acid (Cl<sub>2</sub>DAA) schematically shown in Fig. 1. Cl<sub>2</sub>DAA is a waste product  
42 from bleaching processes in paper mills and pulp effluents and is highly toxic for aquatic organisms  
43 [4].

44

45 The toxicity of RAs against insects, fungi and other organisms is currently linked to their ability to  
46 integrate into the cellular membrane due to their hydrophobicity. The concentrated release of RAs  
47 toward an invading organism or upon tissue damage is suggested to locally induce a toxic RA to  
48 lipid ratio. In particular, toxicological studies showed that RAs' toxicity correlates to the  
49 perturbation of the cellular membrane integrity. Electron paramagnetic resonance was used for *in*  
50 *vitro* assays to study the cytotoxicity of terpenes on erythrocytes showing a clear weakening of the  
51 cell membrane upon exposure to terpenes closely related to the RAs used in this study [5].  
52 Biophysical studies also showed that terpenes, such as abietic acid from the oleo resin, increase  
53 both the permeability and fluidity of the cellular membrane suggesting a more disordered lipid  
54 packing in DPPC and DMPC bilayers [6, 7].

55

56 It is noteworthy that small structural differences in terpenes (for example, a single bond in *cis* or  
57 *trans* conformation or additional functional groups) can lead to major differences in toxicity that  
58 may correlate to their degree of lipid membrane perturbation [8]. However, no systematic studies  
59 investigating the structural effects of RAs on model phospholipid monolayers and bilayers have  
60 been reported to date.

61

62 Here, we study the lipid membrane structure and morphology using both DPPC and soybean polar  
63 lipid extract in admixture with 3 RAs of similar chemical structure, namely natural dehydroabietic

64 acid (DAA) and neoabietic acid (NA), both found in conifer resin, as well as their synthetic  
65 analogue (Cl<sub>2</sub>DAA). Toxicological studies concluded that among natural compounds DAA has a  
66 higher antimicrobial toxicity than NA [9], while another study (that included Cl<sub>2</sub>DAA and DAA)  
67 reported a significantly higher toxicity of chlorinated compounds over non-chlorinated compounds  
68 [10]. The chemical structures of the three RAs and the main phospholipid DPPC used in this study  
69 are shown in Fig. 1.

70

71 Fig. 1. Molecular structures of the three diterpene resin acids (RAs) and the lipid used in this study. Top, from the left:  
72 dichlorodehydroabietic acid (Cl<sub>2</sub>DAA), dehydroabietic acid (DAA) and neoabietic acid (NA). Bottom: the chemical  
73 structure of the main lipid used in this study, Dipalmitoylphosphatidylcholine (DPPC) including the carbon numbering  
74 relevant for the PT ssNMR analysis.

75

76 Specifically, we investigated the effect of RAs on the biophysical properties and structure of both  
77 lipid vesicles and lipid monolayers using a wide range of complementary biophysical techniques.  
78 Differential scanning calorimetry (DSC), polarization transfer solid-state nuclear magnetic  
79 resonance (PT ssNMR), dynamic light scattering (DLS) and cryogenic transmission electron  
80 microscopy (Cryo-TEM) were used to reveal the overall structural effects on DPPC bilayers.  
81 Neutron reflectometry (NR) and the Langmuir trough (LT) were used to investigate changes at the  
82 molecular level and the RAs' localization within the lipid monolayer. The complementarity of these  
83 techniques allowed correlating changes at the vesicle level with changes at the molecular level of  
84 DPPC membranes in the presence of RAs. Additionally, the DLS measurements of polar soy lipid  
85 extract suggest that the effects observed for DPPC also apply to more biologically relevant lipid  
86 mixtures.

87

## 88 **2. Experimental Section**

### 89 **2.1 Materials**

90 The lipids, DPPC, 1,2-dipalmitoyl-d62-*sn*-glycero-3-phosphocholine (d<sub>62</sub>DPPC), 1,2-dipalmitoyl-  
91 *sn*-glycero-3-phosphocholine-N,N,N-trimethyl-d9 (d<sub>9</sub>DPPC) and soybean polar lipid extract  
92 (Composition in wt/wt%: phosphatidylcholine: 45.7, phosphatidylethanolamine: 22.1,  
93 phosphoinositol: 18.4, phosphatidic acid: 6.9 and unknown: 6.9) [11] were purchased from Avanti  
94 Polar Lipids, Inc. (AL, USA) with a purity over 99 %. Tris-buffered saline (TBS) solution  
95 containing 50 mM Tris and 150 mM NaCl at pH of 7.4 was used in all preparations. Cl<sub>2</sub>DAA, DAA

96 and NA were purchased from Orchid, Cellmark (Canada). All other chemicals were obtained from  
97 Sigma Aldrich (Brøndby, Denmark) unless otherwise indicated.

98

## 99 2.1. Vesicle Preparation

100 Vesicles were prepared by manual extrusion. Briefly, lipids and RAs dissolved in chloroform were  
101 mixed at a molar ratio of 9:1 and spread onto the glass vial surface with a glass syringe (Hamilton,  
102 USA), followed by drying under a soft nitrogen stream and subjection for 1 hour under a vacuum to  
103 remove residual organic solvent. Lipid films were used immediately or stored at -20°C. The lipid  
104 film was rehydrated and extruded in buffer well above the melting temperature ( $T_m$ ), which is  
105 reported to be 41°C for DPPC [12] and -63°C [13] for soybean polar lipids. The vesicle suspension  
106 was extruded eleven times through a 100 nm pore size polycarbonate filter membrane using a mini  
107 extruder (Avanti Polar Lipids, Inc.).

108

## 109 2.2. Dynamic Light Scattering (DLS)

110 DLS measurements were performed using an ALV/CGS-3 (ALV- GmbH, Germany) apparatus  
111 containing a Helium-Neon Laser ( $\lambda = 632.8$  nm) to determine the hydrodynamic size of the vesicle  
112 population. The experiment was performed in TBS buffer at a final vesicle concentration of 0.1 mg  
113 lipid/ml. Measurements for each sample were taken out immediately after extrusion ( $h_0$ ) and one  
114 day later ( $h_{24}$ ). Data was collected at a detection angle of  $\theta = 90^\circ$  for 60 seconds. The data was  
115 analyzed with the ALV correlator Software 3.0 (ALV GmbH, Germany).

116

117 For the analysis, the normalized electric field correlation ( $g_1(t)$ ), which describes the measured  
118 intensity fluctuations, is determined by using the distribution of exponential decays

$$119 \quad g_1(t) = \int A(\tau) \exp(-t/\tau) d\tau$$

120 where  $\tau$  is the relaxation time and  $A(\tau)$  its distribution. Therefore, the contribution of a particle to  
121  $A(\tau)$  is proportional to its scattering intensity and thus large particles bias strongly the distribution.  
122 Furthermore, the cooperative diffusion coefficient ( $D_c$ ) relates to  $\tau$  via the relationship

$$123 \quad \tau = (D_c q^2)^{-1}$$

124 with  $q$  as the scattering vector ( $q = 4\pi n/\lambda \sin(\theta/2)$ ). At an infinite dilution  $D_c$  will be reduced to the  
125 self-diffusion coefficient of the particle in solution and therefore links to the hydrodynamic radius  
126 which is calculated by the Stokes- Einstein equation

$$127 \quad D = \frac{kT}{6\pi\eta R}$$

128 with  $T$  as the temperature in Kelvin,  $k$  being the Boltzmann Constant,  $R$  as the hydrodynamic radius,  
129 the solution viscosity ( $\eta = 0.89$  mPa s) as well as the refractive index of water ( $n = 1.33$ ) [14][15].  
130 The DLS data is displayed as relaxation time distributions vs the hydrodynamic radii (nm).

131

### 132 2.3. Cryogenic-Transmission Electron Microscopy (cryo-TEM)

133 Cryo-TEM was applied to visualize the shape and size of the vesicles and aggregates. The imaging  
134 was performed with a Philips CM120 BioTWIN microscope (University of Lund, Sweden) with an  
135 Oxford CT 3500 Cryoholder and transfer system. This instrument gives a high resolution down to  
136 0.34 nm [16]. Solutions with a final vesicle concentration of 1 mg/ml in TBS were prepared one day  
137 prior to the experiment. The samples were prepared by plunge freezing. Briefly, a small drop of the  
138 vesicle solution was transferred to a thin carbon grid and after gently removing the excess liquid,  
139 the sample was rapidly frozen at  $-180^\circ\text{C}$  in an ethane bath. During both, the transfer and the  
140 imaging the samples were kept at  $-150^\circ\text{C}$  using liquid nitrogen. At least 330 vesicles in two  
141 replicates generated from one aliquot were analyzed with the Software ImageJ (National institute of  
142 Health, Maryland, USA) to measure the average diameter without further image treatment.

143

### 144 2.4. Surface pressure - area ( $\pi$ -A) isotherms at the air/water interface

145 Surface Pressure – area ( $\pi$ -A) isotherms were undertaken at the air/water interface on a mini trough  
146 film balance (KSV Instruments Ltd., Finland) with a working surface area of  $144\text{ cm}^2$ . The water  
147 surface was considered to be clean after a total area compression did not lead to a change in surface  
148 pressure of more than  $0.1\text{ mN/m}$ , and the measured  $\pi$  was that of water at  $25^\circ\text{C}$  ( $72\text{ mN/m}$ ) [17].  
149 The lipids and RAs were mixed in chloroform prior use and spread on the water surface to reach a  
150 mean molecular area (MMA) of  $\sim 128\text{ \AA}^2$  for each mixture. The chloroform solution was given 15  
151 minutes to evaporate before the  $\pi$ -A isotherms were measured with a compression speed of  $1\text{ cm}$   
152 per minute at constant temperature. The temperature was controlled with an external water bath. To

153 additionally analyze changes in compressibility of the lipids the compressibility modulus ( $C_s^{-1}$ ) was  
154 calculated using the formula

$$155 \quad C_s^{-1} = -A \left[ \frac{\partial \pi}{\partial A} \right]$$

156 in which  $\pi$  is the surface pressure and A is the MMA at a given point.

157

## 158 2.5 Neutron Reflectometry (NR)

159 Specular neutron reflectometry (NR) was used to analyze the structure of DPPC/RA monolayers at  
160 the air/water interface. NR enables one to obtain structural information perpendicular to the  
161 interface in a non-destructive manner. Two reflectometers were used in this study: FIGARO at the  
162 Institute Laue-Langevin (Grenoble, France) [18] and INTER at the Rutherford Appleton  
163 Laboratories (Didcot, UK) [19] Briefly, an incident “white” neutron beam, with a chosen  
164 wavelength ( $\lambda$ ) generated by a single crystal monochromator, is directed on the air/water interface  
165 and is partially reflected and refracted depending on the incident angle ( $\theta$ ) and  $\lambda$ . The ratio between  
166 incident and reflected beam is then measured as a function of the wave vector defined as  $Q =$   
167  $\frac{4\pi}{\lambda} \sin \theta$ . To obtain detailed structural information the isotropic contrast in the sample is important.  
168 The scattering length density (SLD) determines the isotropic contrast by highlighting different  
169 components in the sample. The SLD is described by the sum of the coherent scattering length  $b_j$   
170 times the number of nuclei in a given volume  $n_j$  ( $SLD = \sum n_j \times b_j$ ). By exchanging hydrogen with  
171 deuterium, the SLD of a molecule can be increased and the isotropic contrast can be manipulated to  
172 partially highlight specific parts of a molecule. In this study, the four isotropic contrasts consisted of  
173  $d_{62}$ DPPC on  $D_2O$ ,  $d_{62}$ DPPC on air contrast matching water (ACMW, 8 w%  $D_2O$ ), hDPPC on  $D_2O$   
174 and  $d_9$ DPPC on ACMW with and without the presence of RA.

175

176 For these experiments, a Langmuir trough with two movable barriers and a total compressible area  
177 of  $605.3 \text{ cm}^2$  was used. The experiments were performed under the same conditions as stated for the  
178  $\pi - A$  isotherms section, adjusted to the larger trough area respectively The measurements were  
179 carried out at  $\pi = 30 \text{ mN/m}$ , which is the estimated lateral pressure of a biological membrane [20].  
180 In the data interpretation procedure, the four isotropic contrasts were simultaneously fitted to get a  
181 unique model. The data was analyzed using the Motofit software, which uses the Abeles matrix for

182 simulations of reflectometry data [21]. The SLD values used in the fitting procedure are  
 183 summarized in table Supporting Information SI 2. Briefly, a two-layer model was applied that  
 184 separates the head group from the acyl chain region of the monolayer. Each layer was given a  
 185 specific SLD. In this way, we determined the thickness and roughness of each layer as well as the  
 186 solvent penetration into the head group. The roughness of each layer was larger or equal to the  
 187 roughness induced by capillary forces 3.7Å (Supporting Information Fig. 1). Specifically, from the  
 188 fitted parameters the hydration ( $\phi$ ) of the head group was calculated using the following  
 189 relationship:

$$191 \quad SLD_{head\ group} = (Layer_{SLD\ ideal} \times (1 - \phi)) + Bulk_{SLD} \times \phi$$

## 193 2.6 Differential Scanning Calorimetry (DSC)

194 DSC experiments were performed using a MicroCal™ VP-DSC system (GE Healthcare Bio-  
 195 Sciences, Sweden). Extruded vesicles (1 mg lipid /ml in TBS) were measured in two thermal cycles  
 196 including heating and cooling from 10 to 70°C at a rate of 1°C per 1.5 minutes and a chamber filled  
 197 with buffer as a reference. Duplicates were analyzed on the VPViewer™2000 (GE Healthcare,  
 198 MA, USA) software. The enthalpy ( $\Delta H^\circ$ ) of the  $L_{\beta'}$  –  $L_{\alpha}$  phase transition was determined by the  
 199 area below the main phase-transition peak of a heating cycle. Additionally, the cooperative unit  
 200 (CU) was calculated using the van't Hoff enthalpy ( $\Delta H_{vH}$ ) for a two state model based on the  
 201 assumption that no significant intermediate populations occur [22].  $\Delta H_{vH}$  is calculated using the  
 202 following relationship:

$$204 \quad \frac{\partial \ln K}{\partial T} = \frac{\Delta H}{\Delta H_{vH} RT^2}$$

206 where K is the equilibrium constant of the  $L_{\beta'}$  –  $L_{\alpha}$  phase transition, R is the gas constant, T is the  
 207 absolute Temperature (Kelvin), and  $\Delta H_{vH}$  is the van't Hoff enthalpy. CU is then defined by the ratio  
 208 of the transition enthalpy and the van't Hoff enthalpy ( $\Delta H_{vH}/\Delta H_{cal}$ ) and displays the amount of  
 209 molecules within one cooperative unit [23].



211 2.7 Polarization transfer solid-state nuclear magnetic resonance (PT ssNMR)

212 For the PT ssNMR studies, 20 mg of fully hydrated DPPC, DPPC/DAA and DPPC/NA samples at a  
213 water to lipid molar ratio of 40:1 were prepared 21 days before the measurement to ensure sufficient  
214 equilibration time. The lipid samples were prepared using TBS buffer and loaded into rotor inserts  
215 that were then placed in a 4 mm Bruker rotor.

216

217 NMR experiments were performed at  $^1\text{H}$  and  $^{13}\text{C}$  resonance frequencies of, respectively, 500 and  
218 125 MHz on a Bruker Avance II 500 spectrometer with a 4 mm  $^{13}\text{C}/^{31}\text{P}/^1\text{H}$  Efree probe. The  $^{13}\text{C}$   
219 signal was recorded under 5 kHz magic-angle spinning (MAS) [24] and 48 kHz two pulse phase  
220 modulation (TPPM) decoupling [25] with 31.25 kHz spectral width and 100 ms acquisition time.  
221 The  $^{13}\text{C}$  chemical shift was referenced to tetramethylsilane using the 43.67 ppm  $\alpha$ -carbon signal of  
222  $\alpha$ -glycine as secondary standard [26]. Hard radiofrequency (RF) pulses were applied at 80 kHz  
223 nutation frequency, giving  $90^\circ$  and  $180^\circ$  pulse lengths of, respectively, 3.1 and 6.2 ms. Direct  
224 polarization (DP) spectra were acquired after a single  $^{13}\text{C}$   $90^\circ$  pulse. Selective enhancement of  
225 resonances from rigid and mobile segments were achieved by the cross polarization (CP) [27] and  
226 insensitive nuclei enhanced by polarization transfer (INEPT) [28] schemes. CP was carried out with  
227 1 ms contact time, 80 kHz  $^{13}\text{C}$  nutation frequency, and linear ramp of  $^1\text{H}$  nutation frequency from  
228 72 to 88 kHz. The INEPT measurements were performed with the delays  $t = 1.2$  ms and  $t' = 1.8$  ms.  
229 Each spectrum was acquired by accumulating 256 transients at 5 s recycle delay. The sample  
230 temperature was controlled with a Bruker BVT unit and calibrated to an accuracy of  $0.2^\circ\text{C}$  with  
231 methanol at 5 kHz MAS [29].

232

233 The data was processed with 20 Hz line broadening, zero-filling from 1560 to 8192 points, Fourier  
234 transformation, automatic phase correction [30], and baseline correction using in-house Matlab  
235 scripts based on matNMR [31]. In order to facilitate observation of transitions between solid and  
236 liquid phases, the DP, CP, and INEPT spectra were overlaid and color-coded in gray, blue, and red,  
237 respectively [32,33]. This set of measurements is known under the term polarization transfer solid-  
238 state NMR (PT ssNMR) and has been applied for studies of phase transitions in a wide range of  
239 aqueous surfactant and lipid systems [33–36].

240

241

### 242 3. Results

243

#### 244 3.1. Formation of large vesicular structures in the presence of RAs

245 DLS and Cryo-TEM were combined to characterize the vesicle size and shape distribution in  
246 samples based on either DPPC or the polar soybean lipid extract with and without 10 mol% RA.  
247 Freshly extruded vesicles and vesicles incubated for 24 h at room temperature (RT) after extrusion  
248 were measured with DLS at 90° (Fig. 2 and Supporting Information Fig. S2 and S3). For DPPC  
249 alone, a monodisperse vesicle population with an average radius of  $70 \pm 4$  nm ( $n=3$ ) with a stable  
250 size distribution over at least 24 h was observed. For polar soybean lipid vesicles, the mean vesicle  
251 size was  $40 \pm 10$  nm both right after extrusion ( $h_0$ ) and after 24 h of incubation at RT ( $h_{24}$ ).  
252 However, the size distribution broadened towards larger vesicles over time (Supporting Information  
253 S2) reflecting higher dynamics of the polar soybean lipid extract due to their higher fluidity as  
254 compared to the more static gel phase DPPC vesicles. Due to these differences, Fig. 2 shows the  
255 DLS data for soy lipid/RA mixtures at  $h_0$ , whereas the DPPC/RA mixtures are presented at  $h_{24}$   
256 to allow for a longer equilibration time and similar extent of mixing for both lipid systems. The  $h_0$  and  
257  $h_{24}$  data sets for DPPC/RA and soybean lipid/RA mixtures are given in Supporting Information Fig.  
258 S3.

259

260 For DPPC vesicles, the presence of RAs led to a broadening and shifting of the vesicle peak  
261 maximum towards smaller sizes already at  $h_0$  (Supporting Information Fig. S3). Over time ( $h_{24}$ ) this  
262 vesicle population was accompanied by the appearance of a second maximum for Cl<sub>2</sub>DAA and  
263 DAA at larger vesicle sizes (Fig. 2A). For DPPC/Cl<sub>2</sub>DAA, the first maximum appeared at  $70 \pm 5$   
264 nm and a second maximum appeared at  $290 \pm 60$  nm. When DAA was added, the first maximum  
265 occurred at  $50 \pm 10$  nm and either a long tail or a second smaller peak appeared at  $380 \pm 60$  nm. For  
266 DPPC/NA vesicles, the maximum in size distribution shifted also to slightly smaller radii ( $60 \pm 3$   
267 nm) at the same time that the peak broadened toward larger vesicles with a maximum radius of  
268  $\sim 130$  nm. Additionally, the DLS detector-counts for a given laser opening remained roughly  
269 constant suggesting that very large aggregates that sediment did not accumulate in DPPC samples.

270

271

272 Fig.2. Impact of resin acids on lipid vesicles prepared from DPPC after 24 hours of incubation at RT (A) and the polar soy lipid  
273 extract immediately after extrusion (B) without (solid line) and with (dotted lines) a given RA (10 mol %). In this figure  $\tau_A(\tau)$  is  
274 plotted as a function of the hydrodynamic size radius (nm) showing qualitatively the appearance of larger vesicular structures in the  
275 presence of RAs.

276  
277 When RAs were added to polar soybean lipid vesicles, a similar effect was observed at  $h_0$  (Fig. 2B).  
278 Specifically, two maxima were observed at radii of  $50 \pm 20$  nm and  $70 \pm 10$  nm when  $Cl_2DAA$  was  
279 incorporated into soybean lipid vesicles. For soybean/DAA vesicles, the maximum in the size  
280 distribution occurred at  $40 \pm 10$  nm and a long tail appeared at higher sizes up to  $160 \pm 30$  nm. For  
281 soybean/NA lipid vesicles, the broadening of the size distribution was also accompanied by a  
282 significant shift in the maximum of the observed vesicle size to  $60 \pm 10$  nm. The soybean lipid  
283 extract vesicles tend to aggregate over time and thus these differences are less clear at  $h_{24}$   
284 (Supporting Information Fig. S2). To sum up, for both DPPC and the polar soybean lipid extract  
285 two of the three RAs lead to the formation of larger vesicular structures suggesting similar  
286 structural effects for the model DPPC/RA, as well as for the more biologically relevant soybean/RA  
287 mixture.

288  
289 Fig. 3. A) Cryo TEM images of DPPC vesicles in the presence of 10 mol% RA: DPPC (1) with 10 mol%, NA (2),  $Cl_2DAA$  (3) and  
290 DAA (4). B) Correlating histograms of maximum vesicle lengths (nm) that were obtained from 330 distinct vesicles.

291  
292 To analyze the reasons behind the increase in vesicle size on the microscopic level, DPPC/RA  
293 vesicles were visualized by Cryo-TEM (Fig. 3A). DPPC vesicles presented rhombic (faceted)  
294 shapes typical for lipid vesicles in the gel phase [37]. The majority of vesicles were unilamellar  
295 with a quite narrow size distribution, as expected due to the extrusion. For DPPC/RA mixtures,  
296 spherical rhombic vesicles were accompanied by smooth tubular structures, which were mainly  
297 found in clusters. To quantify the impact on the length, the maximum diameters of 330 individual  
298 vesicles were measured and the histograms of the corresponding lengths are shown in Fig. 3B. The  
299 vesicle size distribution obtained using Cryo-TEM imaging for DPPC vesicles gave a radius of  $47 \pm$   
300  $17$  nm (Fig. 3B and Fig. 2A). The majority of vesicles in all samples show a maximum diameter at  
301  $\sim 110$  nm and furthermore no DPPC vesicles larger than 250 nm occurred in the absence of RAs  
302 (Fig. 3B). Therefore, all tubular structures with a maximum diameter over 250 nm must be induced  
303 by RAs. The addition of  $Cl_2DAA$  and DAA produced tubular vesicles with a maximum length of  
304 830 nm and 860 nm, respectively. The percentage of vesicle structures above a 250 nm length for  
305  $Cl_2DAA$  was 21%, while that value was 11% and 3% for DAA and NA, respectively. Clearly, the  
306 overall size and structure of most vesicles remained unaffected by RAs. The Cryo-TEM-based size

307 distribution (Fig. 3B) is qualitatively consistent with that produced by DLS (Fig. 2A) and the  
308 presence of larger vesicular structures follows the trend  $\text{Cl}_2\text{DAA} > \text{DAA} > \text{NA}$ . The main  
309 differences in absolute sizes and relative intensities presented from DLS and Cryo-TEM depend on  
310 the physical basis of the techniques used, as DLS measures the size dependent scattering intensities  
311 in bulk solution, while Cryo-TEM allows the evaluation at the single vesicle level.

312

### 313 3.2. Decreased lipid compressibility in the presence of RAs

314 The RA effect on lipid packing in DPPC monolayers was studied using Langmuir ( $\pi$ -A) isotherms  
315 (Fig. 4A). Briefly, the DPPC molecules were added onto the aqueous subphase in the gaseous phase  
316 at  $\pi = 0$ . As  $\pi$  increased, the monolayer underwent a phase transition into the liquid- expanded (LE)  
317 phase up to  $\pi \sim 10$  mN. Then a first order phase transition to the liquid - condensed (LC) phase took  
318 place, during which the LE and LC phases co-existed. The isotherm for DPPC is similar to that  
319 reported earlier under similar experimental conditions [38-39].

320

321 Fig. 4. Impact of RAs on lipid packing in monolayers. A)  $\pi$  - MMA isotherms for DPPC and DPPC/RA (9:1 molar ratio) monolayers  
322 on water. B) Compressibility modulus plot ( $C_s^{-1}$ ) versus surface pressure displaying the compressibility of the mixtures at all points  
323 during compression. The liquid expanded (LE) and liquid condensed (LC) phases are labelled in B for clarity.

324

325 In the presence of RAs, the  $\pi$ -A isotherm of DPPC monolayers shifted to smaller MMA as  
326 compared to the control regardless of the RA type (Fig. 4A). The shift towards smaller MMA  
327 depended on the RA type following the trend:  $\text{Cl}_2\text{DAA} > \text{NA} > \text{DAA}$ . We cannot rule out a loss of  
328 the molecules into the bulk aqueous solution, e.g. in form of mixed lipid/RA micelles, and therefore  
329 we do not further analyze this apparent compaction. However, the slope of the isotherms in the LC  
330 region changed upon RA addition suggesting changes in compressibility. Indeed,  $C_s^{-1}$  decreased in  
331 the LC- phase over  $\pi = 15$  mN/m while the minimum of  $C_s^{-1}$  shifted slightly to a higher surface  
332 pressure for all RAs for DPPC-RA mixtures (Fig. 4B). Overall, our data suggests that RAs integrate  
333 within the phospholipid monolayer inducing structural changes in the lipid packing toward a more  
334 disordered conformation.

335

336 Fig. 5. Structural effects of RAs on DPPC monolayer studied by NR. A) Neutron reflectometry data including the best fits as a  
337 function of the scattering vector ( $RQ^z$ ) for  $d_{62}$ DPPC monolayers with (dotted lines) and without (continuous lines) RAs at the air  
338 water ( $\text{D}_2\text{O}$ ) interface at  $\pi=30$  mN. The profiles are shifted along the y-axis for clarity. B) Scattering length density profiles for the  
339 best fits to the neutron reflection data.

340

341 To determine the structure and composition of the DPPC/RA monolayers, we used NR on  
342 Langmuir films at the air/water interface with four different isotropic contrasts. The reflectometry

343 profiles for d<sub>62</sub>DPPC/RA mixtures on D<sub>2</sub>O changed significantly when RAs were present and, in  
344 particular, the minimum at 0.08 Å<sup>-1</sup> shifted to higher Q following the ranking in this order: Cl<sub>2</sub>DAA  
345 > DAA > NA (Fig. 5A), indicating changes in the overall structure of the monolayer.

346 For the fitting procedure, a two-layer model was applied, dividing the phospholipid monolayer into  
347 a head group layer and the acyl chain. The SLD (Supporting Information Table 1) of either the head  
348 group layer, the acyl chain or both were adjusted during the fitting procedure assuming the presence  
349 of 10 mol % RA to gain information of their co-localization within the DPPC monolayer.  
350 Alternatively, the fitting procedure was carried out under the assumption that no RA is present (see  
351 details in the Supporting Information). The chi<sup>2</sup>-values obtained from the Monte Carlo fitting  
352 method (Supporting Information Fig. S4) allow comparing the quality of the applied models. From  
353 these values, it is likely that both Cl<sub>2</sub>DAA and DAA co-localize within the acyl chain of DPPC.  
354 NA, on the other hand, might co-localize within the head group layer although, in this case, a fit of  
355 similar quality was found assuming the absence of NA in the film. The SLD profiles from the best  
356 d<sub>62</sub>DPPC/RA fits to the NR data in Fig. 5A are shown in Fig. 5B. All other isotropic contrasts are  
357 displayed in the Supporting Information Fig. S4. Table 1 lists the main parameters used for the best  
358 fits shown in Fig. 4B and Supporting Information Fig. S4. The structural parameters for pure DPPC  
359 are in agreement with previous studies at similar  $\pi$  [38][39]. Cl<sub>2</sub>DAA reduced the solvent  
360 penetration in the head group from 15 ± 5 to 6 ± 4 % and decreased the length of the tail from 16.2  
361 ± 0.2 to 14.7 ± 0.1 Å, indicating an increase of the lipid tail tilt ( $t$ ) using the relationship  $\cos(t) =$   
362  $\frac{L}{L_{CH}}$  with  $L$  as the measured acyl chain length and  $L_{CH}$  as the maximal tail length [40]. When DAA  
363 was added to DPPC, the head group hydration and thickness decreased slightly, though within the  
364 fit error. DAA had no effect on the acyl chain tilt, whereas it decreased slightly for NA (the tail  
365 length decreased to 15.6 ± 0.1 Å). The roughness at the head group - tail interface was only  
366 increased by Cl<sub>2</sub>DAA, from 3.7 ± 0.2 to 6.0 ± 0.2 Å.

367  
368 Deuteration effects are known to affect the phase transition in lipids and the dynamics of molecules.  
369 In particular, the main phase transition from L<sub>α</sub> to L<sub>β</sub> decreases by 4 °C per tail for phospholipids  
370 due to deuteration [41]. The NR experiments were performed well below this phase transition and  
371 therefore we expect a similar order within the lipid chains. A small deviation may exist in the exact  
372 conformation of tails and their dynamics, however it is reasonable to assume that these differences  
373 are minor. Indeed, similar thermotropic effects using DSC were observed for RA on hydrogenated

374 or deuterated DPPC (Supporting Information Fig. S6 and Fig. 6). Further comparison of  
375 hydrogenated versus deuterated lipids could be performed by molecular dynamic simulations, but  
376 that remains out of the scope of the present work.

377

378 Table 1. Parameters used for the best the NR fits using a two layer model on DPPC/RA monolayer at 30 mN/m: lipid tail layer  
379 thickness, head group layer thickness, roughness between the head and the tail region. The head solvent penetration of DPPC is  
380 calculated in percentage (%) at  $\pi = 30$  mN/m as described in section 2.5 [42]. The errors were calculated using the Monte Carlo  
381 method embedded in Motofit [43].

382

### 383 3.3 Reduced cooperativity of the DPPC phase transition after RA integration

384 DSC (Fig. 6) and PT ssNMR (Fig. 7-8) experiments were performed to investigate the influence of  
385 RAs on the phase behavior as well as the molecular conformation of DPPC (Fig. 6 - 9). For DSC,  
386 vesicles were first well equilibrated above the melting temperature of DPPC and then subjected to 2  
387 heating/cooling cycles yielding similar thermograms after extrusion (Supporting Information Fig.  
388 S6). The similarity between the heating thermograms of both heating cycles suggests that the  
389 samples were at equilibrium and did not show de-mixing during or prior to the re-heating cycles.  
390 The total heat excess during the main phase transition or the calorimetric enthalpy ( $\Delta H$ ) was  
391 calculated upon integration under each phase transition peak (Table 2). Additionally,  $\Delta H_{\text{vH}}$  and the  
392 cooperativity unit, CU are given in Table 2.  $\Delta H_{\text{vH}}$  corresponds to a simple two state model, while  
393  $\Delta H$  includes all changes independently of the model. Therefore, it is possible to calculate CU using  
394 these two values to asses information about the cooperativity of the main phase transition from the  
395 solid crystalline phase to the fluid phase, which has been thoroughly discussed in the literature [23].

396

397

398 Fig 6. Representative phase transition profiles of vesicles composed of DPPC and DPPC/RA (9:1, mol%). The enthalpy (cal/mole/C)  
399 is plotted as a function of the temperature for pure DPPC (solid line), DPPC/DAA (dotted broken line), DPPC/NA (broken line) and  
400 DPPC/Cl<sub>2</sub>DAA (dotted line).

401

402

403 The DPPC profile in Fig. 6 shows the characteristic pre-transition onset of  $\Delta H \sim 490$  cal/mol/°C at  
404 31°C. This peak corresponds to the transition from the planar gel phase ( $L_{\beta'}$ ) to the rippled gel  
405 phase ( $P_{\beta'}$ ). At 41°C, DPPC underwent a phase transition from the  $P_{\beta'}$  to the liquid crystalline  
406 phase with  $\Delta H \sim 12$  kcal/mol/°C. The melting temperature ( $T_m$ ) is derived as the maximum of the  
407 main transition peak. The sharpness of the peak indicates a highly cooperative phase transition  
408 typical for DPPC (CU = 44). Vesicles containing RA showed both peak broadening and a dramatic  
409 decrease of the maximum of the main phase transition enthalpy. This suggests a loss in

410 cooperativity. Additionally, the pre-transition peak displaying the  $L_{\beta} - P_{\beta}$  transition did not occur  
411 in the presence of RAs. For 10 mol%  $Cl_2DAA$ ,  $\Delta H$  decreased from 12.2 to 5.8 kcal/mol/°C and  
412 increased for DAA and NA to 14.2 and 17.9 kcal/mol/°C. Moreover, for NA and DAA, there was a  
413 significant shift in  $T_m$  from 41°C to 38°C. Thus, all RAs led to a decrease in cooperativity of the  
414 main phase transition of DPPC as indicated by the increase in CU. Note that CU decreased for 5  
415 mol%  $Cl_2DAA$  from 44 to 27, but increased to 52 for 10 mol%. Such increase in CU is an artefact  
416 produced from the decrease of the transition peak for DPPC/ $Cl_2DAA$  compared to pure DPPC. The  
417 peak does not seem to broaden due to the loss of width at the same time. As a consequence, the  
418 width-height ratio suggests a cooperative phase transition. However, the data irrevocably indicate a  
419 drastic perturbation of the lipid packing for this particular RA.

420

421 Table 2.  $\Delta H$ ,  $\Delta H_{vH}$ , CU and  $T_m$  values for DPPC and DPPC/RA vesicles.  $\Delta H$  and  $T_m$  were directly calculated from the  
422 heat excess measured by the DSC, whereas  $\Delta H_{vH}$  and CU were calculated as stated in the methodological section.

423

424 PT ssNMR data was collected for DPPC and DPPC mixtures in the lamellar phase containing 10  
425 mol % NA or DAA for a detailed analysis of the phase transition. Fully hydrated DPPC and binary  
426 mixtures were investigated well below the phase transition at 25 °C in the  $L_{\beta}$  phase, above the  
427 melting point at 50 °C in the fluid lamellar phase, and at intermediate temperatures. In this way, the  
428 dynamics of different segments in DPPC can be followed throughout the entire melting process.  
429 The  $^{13}C$  MAS NMR spectra display the data from experiments including the DP, INEPT and CP  
430 signals (Fig. 7).

431

432 For the  $L_{\alpha}$  phase, the excellent resolution of the  $^{13}C$  chemical shifts affords separate observation of  
433 each of the carbons of the choline moiety of the head group ( $\alpha$ ,  $\beta$  and  $\gamma$ ), the glycerol backbone ( $g_1$ ,  
434  $g_2$ , and  $g_3$ ), as well as several carbons of the acyl chains (1, 2, 3, 14, 15, and 16). The central  
435 segments of the acyl chains (4-13) give rise to a cluster of overlapping resonances at 30-32 ppm.  
436 The peak maximum at 31 ppm is indicative of a distribution of *trans* and *gauche* conformations  
437 typical of liquid hydrocarbons [36]. The signal amplitudes obtained with CP and INEPT can be  
438 rationalized in terms of the correlation time  $t_c$  and order parameter  $S_{CH}$  quantifying the rate and  
439 anisotropy of CH bond reorientation [33]. Intense INEPT and vanishing CP indicates fast isotropic  
440 reorientation (approximately  $t_c < 10$  ns and  $|S_{CH}| < 0.01$ ) characteristic of liquids with low viscosity.

441 Conversely, strong CP without INEPT can be observed for solids ( $t_c > 0.1$  ms). Anisotropic liquids  
442 ( $t_c < 10$  ns and  $0.05 < |S_{CH}| < 0.2$ ) give rise to INEPT and CP signals with similar amplitudes.

443 The 45 °C data for all samples are characteristic of  $L_\alpha$  phases with INEPT signals indicating fast  
444 reorientation of all segments ( $t_c < 10$  ns). The absence of CP for the carbons of the  $CH_3$  groups 16  
445 and g show that these segments undergo isotropic reorientation. The comparable CP and INEPT  
446 amplitudes for most carbons verify that the phase is anisotropic.

447 At 25 °C, CP signals dominate for all samples consistent with the expected solid phases. Notable  
448 exceptions are the INEPT signals for the carbons g, and to some extent  $\alpha$  and  $\beta$ , indicating that the  
449 choline moiety remains mobile even below the solid-to-liquid phase transition. The 33 ppm shift of  
450 the peak from the central segments of the acyl chains is a signature of an all-*trans* conformation.  
451 Taken together, these observations are consistent with an  $L_\beta$  phase with all-*trans* acyl chains and  
452 hydrated head groups.

453

454 According to the DSC data, the pure DPPC sample transforms from  $L_\beta$  to  $P_\beta'$  at 33 °C. In the NMR  
455 data, this transition is mainly observed as a minor increase in the linewidth of the 33 ppm peak  
456 consistent with subtle differences in acyl chain packing for the troughs and ridges of the  $P_\beta'$  phase.  
457 The transition from  $P_\beta'$  to  $L_\alpha$  gives rise to the appearance of INEPT signals for all carbons. The  
458 two-phase data at 37 °C is a superimposition of the one-phase  $P_\beta'$  and  $L_\alpha$  data at 35 and 39 °C,  
459 respectively. In particular, the peaks at 33 and 31 ppm show the coexistence of acyl chains in two  
460 distinct states: solid-like all-*trans* conformation and a liquid-like distribution of *trans*- and *gauche*  
461 conformations. For both RA samples, the transition from  $L_\beta$  to  $L_\alpha$  is more continuous and lacks a  
462 clear two-phase region (Fig. 7 at 37 °C). Rather than having two pronounced maxima for the main  
463 acyl chain peak, there is a smooth transition between the shifts characteristic for the low and high  
464 temperature states.

465 Both, DSC and ssNMR data suggest that DPPC undergoes a phase transition at lower temperatures  
466 in the presence of DAA and NA. Data in Fig. 7 for DPPC and the DPPC/RA mixtures at 35 °C  
467 degrees displays the differences in the flexibility of the acyl chains at this temperature. Supporting  
468 Information Fig. S8 shows the expanded area from 20 – 40 ppm corresponding to  $C_{2-15}$ . The spectra  
469 for DPPC show no INEPT signal for any chain segment indicating that DPPC exists in its solid  
470 phase. Moreover, the peak at 32.8 ppm as well as the broadness of the CP signal for these peaks  
471 indicate an all-*trans* conformation for  $C_{4-13}$  and thus support the gel phase for DPPC [44]. For DAA  
472 and NA, the spectra clearly showed INEPT signals and rather distinct peaks. The chemical shifts for



473 C<sub>2-15</sub> appear at 31.4 ppm and 31.6 ppm for DAA and NA, respectively, suggesting an ongoing phase  
474 transition. Overall, the data confirm a lower phase transition of DPPC/RA mixtures regardless of  
475 RA type, thus agreeing with the DSC data (Fig. 6). For future experiments it would be interesting to  
476 study detailed effects on the flexibility of certain segments in DPPC caused by Cl<sub>2</sub>DAA for  
477 comparison.

478

479 Fig. 7. <sup>13</sup>C MAS NMR spectra (DP: gray; CP: blue; INEPT: red) of DPPC (A) and DPPC with 10 mol% DAA (B) and NA (C) from  
480 25 to 50°C in the lamellar phase. Insets: Magnification of the spectral region of the lipid tails. The spectra were obtained with 125  
481 MHz <sup>13</sup>C frequency, 5 kHz MAS and 48 kHz TPPM decoupling.  
482

483 On the other hand, we observed different conformations of DPPC segments upon NA integration in  
484 the gel phase at 25 °C. The <sup>13</sup>C MAS NMR spectrum showed the appearance of a sharp CP peak at  
485 14.13 ppm for the C<sub>16</sub> methyl terminus at trans conformation in DPPC (Fig. 8A), whereas this peak  
486 broadened for DAA (Fig. 8B) and split in the presence of NA (Fig. 8C). Moreover, differences were  
487 observed for the C<sub>α</sub> located in the head group at 59.3 ppm for NA only. This peak appeared as a  
488 sharp INEPT signal at 59.3 ppm, indicating fast ( $\tau_c < 10$  ns) reorientation of the DPPC head groups  
489 (Fig.8).

490

491 Fig. 8. <sup>13</sup>C MAS NMR spectra (DP: gray; CP: blue; INEPT: red) of DPPC (A) and DPPC with 10 mol % DAA (B) and NA (C) at 25  
492 °C. The spectra were obtained with 125 MHz <sup>13</sup>C frequency, 5 kHz MAS and 48 kHz TPPM decoupling. \* Peaks corresponding to  
493 TRIS, which is used in the buffer.  
494

#### 495 **4. Discussion**

496 In this study, we performed DLS, PT ssNMR, NR, DSC, Cryo-TEM experiments on DPPC  
497 vesicles, monolayer and lamellar phase as well as DLS experiments on vesicles composed of the  
498 biologically relevant polar soybean lipid extract to unravel structural effects of three closely related  
499 RAs on a phospholipid bilayer. Furthermore, we determine the co-localization and of these RAs  
500 within DPPC monolayer and correlate changes on DPPC to the RAs toxicity.

501

502 DLS enabled us to obtain qualitatively comparable data for both model systems. Our DLS results  
503 (Fig. 2) suggest that RAs induce similar structural alterations on the size distribution of lipid  
504 vesicles for DPPC and the polar soy lipid extract. We found that DPPC/RA mixtures in the gel  
505 phase showed the formation of larger structures after 24 hours. In contrast, the liquid crystalline soy  
506 lipid/RA mixtures showed immediate effects on the vesicle sizes and signs of further vesicle growth

507 and accumulation after 24 hours. Therefore, the two lipid model systems are compared at two  
508 different time points to show similar extents of mixing as the dynamics of the system are expected  
509 to be different for fluid and gel membranes. By comparing the two model systems it can be  
510 concluded that Cl<sub>2</sub>DAA and DAA induce major structural changes within phospholipid vesicles  
511 leading to significantly larger vesicle sizes, whereas the effect of NA led to a small increase in  
512 vesicle size distribution.

513 The DLS data was confirmed by Cryo-TEM that allowed visualizing elongated vesicles with  
514 lengths up to 250 nm for DPPC/RA mixtures for Cl<sub>2</sub>DAA and DAA but not for NA (Fig. 3). NA led  
515 to slightly larger faceted vesicles suggesting minor effects on the structure of lipid vesicles. The  
516 tubular vesicles were mainly found in clusters, especially for Cl<sub>2</sub>DAA. The clusters could be  
517 produced during the immobilization of the vesicles on the carbon grid due to the water removal.  
518 Besides mechanical causes, vesicle clustering occurs e.g. due to a decreased ability for hydrogen  
519 bond networking between the head groups and the bulk water as well as changes in the longer range  
520 hydration forces. Lower ability to hydrogen bonding is known to reduce the interlamellar space  
521 between bilayers and to increase intervesicular attraction as reported earlier using Raman scattering  
522 microscopy on 1- palmitoyl-2-oleoyl-sn-glycero-3-phosphocholine (POPC) bilayer [45]. The  
523 formation of microtubules suggests a significant change in the lipid packing. Previously, this type  
524 of membrane shape transformation was discussed in connection to peptides interacting with lipid  
525 bilayers [46]. Briefly, both the total interfacial area and acyl chain volume can be kept constant  
526 upon stretching a bilayer tubule as long as the diameter of the tubule decreases proportionally to the  
527 increase in vesicle length. However, the further bending of the lipid bilayer to form highly curved  
528 vesicles imposes a strain on a symmetric bilayer as the inner monolayer has a negative curvature,  
529 while the outer has a positive curvature. By changing the number or type of molecules in the inner  
530 relative to the outer monolayer of the vesicle bilayer, the relative area of the two monolayers will  
531 change although the total area in the bilayer remains constant. This could be achieved, for instance,  
532 by in plane phase separation within the vesicle membrane as observed for cardiolipin rich domains  
533 on the poles of *E.coli* [47]. Tubular structures were also observed earlier for milk fat globule  
534 membranes, composed by lipids with different packing parameters using Cryo-TEM [48]. However,  
535 the formation of highly curved areas does not directly correlate alone to phase separation within a  
536 phospholipid bilayer.

537 Despite the appearance of tubules, the structure of most vesicles in all DPPC/RA mixtures remained  
538 unaffected. This suggests that RAs distribute heterogeneously at the single vesicle level. This

539 heterogeneity is further supported by the PT ssNMR data showing a split of the peak for the acyl  
540 terminal methyl group for DPPC in the lamellar gel phase when NA was added (Fig. 8). Thus,  
541 DPPC exists in two distinguishable conformations upon the integration of NA at 25 °C in the gel  
542 phase. However, for spherical/faceted vesicles the presence of RAs cannot be excluded, yet, the RA  
543 concentration within these vesicles could be too low to alter the vesicle shape. Earlier studies have  
544 shown that compositional heterogeneity at the single vesicle level exists for binary lipid mixtures  
545 using atomic force microscopy [49] and fluorescence microscopy by the inclusion of two lipid  
546 fluorophores [50].

547

548 To further investigate packing effects of RAs on DPPC, Langmuir isotherm experiments were  
549 performed on the lipid monolayer. Our Langmuir data indeed confirmed changes in lipid packing  
550 upon RA insertion in the DPPC monolayer towards reduced compressibility in the LC-phase and a  
551 shift toward smaller MMA for all RAs (Fig. 4). The shift toward smaller MMA could be due to  
552 partial loss of lipid/RA molecules into the aqueous subphase and is therefore not further discussed.  
553 Partial material loss may also influence the reduction in compressibility. However, all RAs reduced  
554 the LE-LC coexisting region displayed by the shortened plateau at  $\pi = 15$  mN/m in the isotherm  
555 (Fig. 4A) and shifted the minima in the compressibility moduli to higher  $\pi$  (Fig. 4B). This suggests  
556 a delay in the formation of the LC phase due to RA integration. To gain certainty about this effect,  
557 Brewster angle microscopy may visualize this expanding effect on DPPC monolayer in future  
558 experiments, as done in the past on pulmonary surfactants protein on lipid monolayer [51]. We note  
559 that the LC – LE plateau did not entirely disappear, which may facilitate a non-homogeneous  
560 distribution of RAs in the DPPC monolayer. Such a non-homogeneous effect could correlate well  
561 with the heterogeneous structural consequences at the bilayer level observed via Cryo-TEM and PT  
562 ssNMR (Fig. 3, 7-8). Although it has to be noted that the comparison between bilayer and  
563 monolayer systems does not necessarily yield similar effects due to the constraints imposed by the  
564 air-water interface.

565

566 In a recent study, a DPPC monolayer mixed with the monoterpene thymol were studied under  
567 similar conditions to the ones used in this work [52]. The authors observed similar changes in the  $\pi$ -  
568 A isotherms as the ones we report here in terms of compressibility modulus and concluded that the  
569 terpenes clearly had a fluidizing effect on DPPC monolayers. Our DSC and PT ssNMR data

570 confirmed the changes in membrane fluidity of DPPC bilayer in the presence of RAs (Fig. 6 and 7).  
571 DAA and NA caused the earlier onset and broadening of the  $L_{\beta}$ - $L_{\alpha}$  phase transition of DPPC. The  
572 earlier onset of the phase transition was visible at 35 °C in the  $^{13}\text{C}$  MAS NMR spectra due to the  
573 INEPT signal, the shift from 32.8 to 31.4 ppm and a clear distinction of the peaks. Similar effects  
574 were recently observed when linear monoterpenes were analyzed in DMPC membranes using PT  
575 ssNMR [35]. Furthermore, the DSC results reveal a drastic loss of cooperativity (CU decrease) of  
576 the phase transition that follows the trend  $\text{Cl}_2\text{DAA} > \text{DAA} > \text{NA}$  (Table 2). The integration of RAs  
577 into DPPC bilayers could destabilize the DPPC crystalline phase in such a way that the forces in the  
578 lattice are lowered to an extent that prevents a cooperative phase transition. Such an effect may be  
579 accompanied with an increased mobility of the acyl chains and is supported by the small decrease in  
580  $T_m$ . This suggests a major disturbance of the lipid packing consistent with an increased disorder of  
581 lipid configurations (Table 2). The increased molecular disorder is supported by: 1) the decreased  
582 compression modulus observed in our monolayer studies (Fig. 4) and 2) coexisting DPPC  
583 configurations in our PT ssNMR data (Fig. 8) for DPPC bilayer. Similar impact on the thermotropic  
584 behavior of lipids as studied by DSC, were reported for abietic acid/DPPC [7] and rosmarinic  
585 acid/DMPC systems (their chemical structure is related to the ones used in this study) [6]. Such  
586 perturbing effect on the thermotropic behavior of lipid membranes for RAs was previously linked to  
587 their toxicity [53]. Our data also suggests that besides the correlation between the toxicity of RAs  
588 and the thermotropic effect on the main phase transition of DPPC, there is a correlation with the  
589 presence of coexisting lipid configurations at 25 °C for NA and the ability to induce highly curved  
590 elongated vesicular structures for DAA and  $\text{Cl}_2\text{DAA}$ .

591

592 For structural details, NR measurements were taken out on Langmuir films to study the molecular  
593 geometry of DPPC/RA monolayer at the air-water interface. The best fit for DPPC monolayers  
594 containing  $\text{Cl}_2\text{DAA}$  and DAA was achieved when these particular RAs were co-localized in the  
595 acyl chain region (Supporting Information Fig. S4). The overall geometry of DPPC changed upon  
596  $\text{Cl}_2\text{DAA}$  integration in terms of a decreased acyl chain length thickness from  $16.2 \pm 0.2$  to  $14.4 \pm$   
597  $0.1 \text{ \AA}$  and increased roughness from  $3.7 \pm 0.2 \text{ \AA}$  to  $6.0 \pm 0.2 \text{ \AA}$  at the head to tail interfacial region  
598 (Table 1). These effects confirmed changes in the lipid packing toward a more disordered lipid  
599 packing, and the integration of this particular RA into the lipid tail region. DAA, which differs from  
600  $\text{Cl}_2\text{DAA}$  only in the absence of the two chlorine atoms, seemed also to co-localize within the acyl  
601 chain, yet there were no effects on the acyl chain length or any further interfacial roughening. These

602 differences may be caused by the presence of the two bulky chlorine atoms in Cl<sub>2</sub>DAA leading to a  
603 drastic perturbation in the acyl chain packing due to their large van der Waals radii and steric  
604 effects they may induce. The main effect caused by DAA on DPPC was the shortening of the head  
605 group region. In contrast, NA is likely to integrate into the head group region of DPPC as  
606 determined by NR (Supporting Information Fig. S4). A fit to the NR data of similar quality could be  
607 found assuming that NA was absent from the Langmuir monolayer. This could be due to lower  
608 contrast between the NA and DPPC head groups or that the actual NA concentration in the  
609 Langmuir film was lower than the nominal composition due to NA molecules being expelled into  
610 the aqueous phase. However, the effects in Langmuir film compressibility, PT ssNMR signals, and  
611 the low aqueous solubility of 2.31 mg/L suggest that NA is indeed kept in the lipid layer [54]. The  
612 best fits to the NR data showed minimal effects on the head group and a slight decrease in the acyl  
613 chain thickness from  $16.2 \pm 0.2$  to  $15.6 \pm 0.1$  Å. This was accompanied by a slight increase in  
614 solvent penetration into the head group region from  $15 \pm 5$  to  $21 \pm 5$  %, although within the fit error  
615 (Table 1). Our PT ssNMR results indeed support increased mobility of the DPPC head group region  
616 as displayed by the INEPT peak for the C<sub>α</sub> carbon (Fig. 9). This INEPT signal in the <sup>13</sup>C MAS  
617 spectra shows all head groups in a mobile conformation at this particular position, which may be  
618 caused by the integration of NA. Furthermore, NA affected the acyl chain, since the CP signal at  
619 14.3 ppm split indicating the terminus methyl group in the acyl chain to exist in two different  
620 conformations or environments (Fig. 8): either as two distinct solid phases, as a single phase with  
621 two distinct locations of the DPPC molecules, or as a single phase where all DPPC molecules are  
622 equivalent but with different conformations of the sn1- and sn2- termini. Thus, it is likely that NA  
623 co-localizes in the head group region of DPPC.

624

625 In summary, the formation of tubular vesicular structures correlates with the suggested co-  
626 localization of RAs in the acyl chain region of DPPC and increased conformational disorder in the  
627 lipid bilayer. The data suggests that RAs may induce a change in the packing parameter. The critical  
628 packing parameter (P) is calculated by

629 
$$P = \frac{V}{S_o l_c}$$

630 where  $V$  is the molecular volume,  $S_o$  is the surface cross section of the head group and  $l_c$  is the  
631 length of the acyl chain [55]. For NA, where no incorporation on the lipid tail occurs, increased

632 mobility in the head group suggests an increased head group area that seems to be compensated by  
633 the tilting of the DPPC chain to maintain a packing parameter close to 1 and therefore the spherical,  
634 faceted vesicle structure prevailed. For DAA and Cl<sub>2</sub>DAA, on the other hand, the incorporation  
635 into the acyl tail is more likely to induce a shift of the packing parameter towards smaller values  
636 and the possibility to accommodate for the highly curved poles of the tubular vesicles. Similar space  
637 filling models have been proposed earlier that show the changes in lipid packing to optimize the van  
638 der Waals forces between lipids and structural consequences for the lipid shape [56]. More recently,  
639 fluorescence microscopy was used to show that cardiolipin, a cone inverted lipid present in *E. coli*,  
640 enriches the regions of *E. coli* with high curvature such as poles and septa [47]. Note that Langmuir  
641 isotherms and NR experiments are performed at the air-water interface, and therefore the studies are  
642 made on lipid monolayers. This may impose an additional constraint against the induction of high  
643 curvature structures due to changes in *P*. This is in contrast to the other techniques in this work  
644 performed on lipid vesicles, which can respond to changes in *P*. Schematics of our proposed model  
645 for RA incorporation into the membrane and its effect on the overall structure of lipid bilayers are  
646 shown in Fig. 9.

647

648 Fig. 9. Proposed impact of the integration of different RAs, NA (blue) and DAA (yellow), on the structure of the DPPC bilayer and  
649 the consequences for the macrostructure of unilamellar vesicles. DAA co-localizes within the lipid tail region, whereas NA co-  
650 localizes at the head-tail interface both affecting the lipid packing to different extents. The higher polarity and/or increased rigidness  
651 of DAA (and bulkiness of Cl<sub>2</sub>DAA) may be responsible for changes in the lipid packing affecting the curvature at the vesicle  
652 level and this, in turn, can be correlated with the increased toxicity of these particular RAs.

653

## 654 5. Conclusion

655 RAs integrate into phospholipid membranes and induce significant effects on the thermotropic and  
656 structural properties of lipid bilayers. The extent in which the DPPC packing parameter is affected  
657 follows the trend Cl<sub>2</sub>DAA > DAA > NA. This trend follows the polarity of these RAs, which can be  
658 displayed by their dipole moment: Cl<sub>2</sub>DAA (3.1 D) > DAA (1.9 D) > NA (1.7 D) [57]. Moreover,  
659 this trend follows each RA's molecular mobility. Briefly, the chemical difference between Cl<sub>2</sub>DAA  
660 and DAA are two synthetically added bulky chlorine atoms at C<sub>14</sub> and C<sub>12</sub>. Due to the relatively  
661 large van der Waals radius of chlorine, the chlorine atoms may cause steric fixation and loss of  
662 flexibility within the molecule, especially on the isopropane group. Both, Cl<sub>2</sub>DAA and DAA share  
663 an aromatic ring with a planar ring geometry in contrast to NA [58]. Moreover, the presence of the  
664 aromatic ring ( $\pi$ - $\pi$  stacking) and chlorine groups increase the polarizability of Cl<sub>2</sub>DAA and DAA as

665 compared to NA. The extent of these effects can be correlated to the toxicity of RAs. More  
666 specifically, we have shown that the more toxic DAA and Cl<sub>2</sub>DAA co-localize in the lipid tail  
667 region and therefore induce mainly changes in this region that lead to alterations in the membrane  
668 fluidity, curvature and shape. Particularly, Cl<sub>2</sub>DAA with two relatively large chlorine atoms  
669 perturbs the interface between the head group and tail region of lipid monolayers due to roughening  
670 of the membrane and a reduction of the head group hydration showing the strongest effects on  
671 phospholipid bilayer structure. This promotes the stretching of the phospholipid membrane and the  
672 formation of tubular vesicular structures. In contrast, the least toxic NA, has its main effects on the  
673 head group region enabling the compensation of perturbing effects by the acyl chain tilt. NA is the  
674 least polarizable and most flexible of the RA studied, and it can be incorporated in the membrane,  
675 to a larger extent, without compromising the functionality of the lipid membrane.

676

#### 677 **Graphical abstract**

678 Same as Figure 9.

679

#### 680 **Acknowledgement:**

681 The authors wish to thank the Institute Laue Langevin (France) and ISIS at the Rutherford  
682 Appleton Laboratory (UK) for allocated beam times and in particular Max Skoda (ISIS) for  
683 excellent local support. We thank Dr. Gunnel Karlsson for great technical support during CRYO-  
684 TEM imaging, Prof. Kell Mortensen for access to DSC (University of Copenhagen) and Göran  
685 Carlström for technical support during NMR (Lund University). We acknowledge funding from the  
686 Swedish Research Council, DANSCATT Centre (Danish government), the Research Centre  
687 ‘bioSYNergy’ funded by the UCPH Excellence programme for interdisciplinary Research and the  
688 Innovation Fund Denmark via the project “Plant Power: Light driven synthesis of complex  
689 terpenoids using cytochrome P450s”.

690

691

692

693

**References**

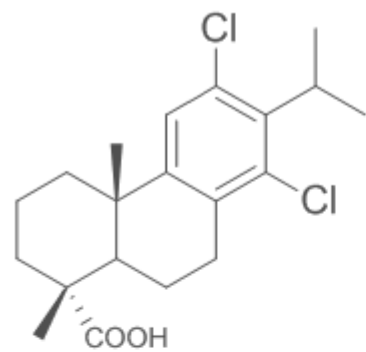
- 695 [1] C.I. Keeling, J. Bohlmann, Diterpene resin acids in conifers., *Phytochemistry*. 67 (2006)  
696 2415–23. doi:10.1016/j.phytochem.2006.08.019.
- 697 [2] S. Savluchinske Feio, B. Gigante, J. Carlos Roseiro, M.J. Marcelo-Curto, Antimicrobial  
698 activity of diterpene resin acid derivatives, *J. Microbiol. Methods*. 35 (1999) 201–206.  
699 doi:10.1016/S0167-7012(98)00117-1.
- 700 [3] H.R.Lerner, *Plant Responses to Environmental Stresses: From Phytohormones to Genome*  
701 *Reorganization*, 1999.
- 702 [4] A.K. Choudhary, S. Kumar, C. Sharma, Removal of Chlorophenolics From Pulp and Paper  
703 Mill Wastewater Through Constructed Wetland, *Water Environ. Res.* 85 (2013) 54–62.  
704 doi:10.2307/42569408.
- 705 [5] S. a. Mendanha, S.S. Moura, J.L. V Anjos, M.C. Valadares, A. Alonso, Toxicity of terpenes  
706 on fibroblast cells compared to their hemolytic potential and increase in erythrocyte  
707 membrane fluidity, *Toxicol. Vit.* 27 (2012) 323–329. doi:10.1016/j.tiv.2012.08.022.
- 708 [6] L. Pérez-Fons, F.J. Aranda, J. Guillén, J. Villalaín, V. Micol, Rosemary (*Rosmarinus*  
709 *officinalis*) diterpenes affect lipid polymorphism and fluidity in phospholipid membranes,  
710 *Arch. Biochem. Biophys.* 453 (2006) 224–236. doi:10.1016/j.abb.2006.07.004.
- 711 [7] F.J. Aranda, J. Villalaín, The interaction of abietic acid with phospholipid membranes.,  
712 *Biochim. Biophys. Acta.* 1327 (1997) 171–80.  
713 <http://www.ncbi.nlm.nih.gov/pubmed/9271259>.
- 714 [8] S. Ali, S. Minchey, a Janoff, E. Mayhew, A differential scanning calorimetry study of  
715 phosphocholines mixed with paclitaxel and its bromoacylated taxanes., *Biophys. J.* 78 (2000)  
716 246–256. doi:10.1016/S0006-3495(00)76588-X.
- 717 [9] T.A. Söderberg, R. Gref, S. Holm, T. Elmros, G. Hallmans, Antibacterial Activity of Rosin  
718 and Resin Acids in Vitro, *Scand. J. Plast. Reconstr. Surg. Hand Surg.* 24 (1990) 199–205.  
719 doi:10.3109/02844319009041279.
- 720 [10] N. Cherr, M. Shenker, Toxic effects of selected bleached kraft mill effluent constituents on  
721 the sea urchin sperm cell, *6* (1987) 561–569.
- 722 [11] index @ [www.avantilipids.com](http://www.avantilipids.com), (n.d.).  
723 [https://www.avantilipids.com/index.php?option=com\\_content&view=article&id=415&Itemid=124&catnumber=541602](https://www.avantilipids.com/index.php?option=com_content&view=article&id=415&Itemid=124&catnumber=541602).
- 724
- 725 [12] K. Jacobson, D. Papahadjopoulos, Phase transitions and phase separations in phospholipid  
726 membranes induced by changes in temperature, pH, and concentration of bivalent cations.,  
727 *Biochemistry*. 14 (1975) 152–161. doi:10.1021/bi00672a026.
- 728 [13] A.P. Lipids, Avanti Polar Lipids Inc., Material Safety Data Sheet, (2015).  
729 <http://avantilipids.com/MSDS/msds.php?ProdNum=880126P&format=raw>.
- 730 [14] D.J. McClements, E. Vittadini, Y. Vodovotz, Understanding and Controlling the  
731 Microstructure of Complex Foods, *Underst. Control. Microstruct. Complex Foods.* (2007)  
732 89–112. doi:10.1533/9781845693671.1.89.
- 733 [15] F. Kreith, *CRC Handbook of Thermal Engineering*, CRC Press, 2010.  
734 <https://books.google.com/books?id=M0NgOBAYmCkC&pgis=1> (accessed March 13, 2015).



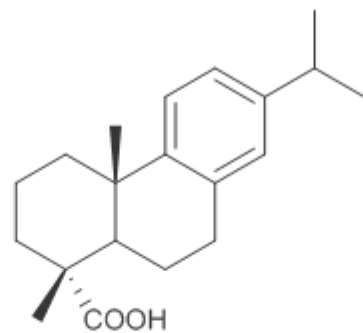
- 735 [16] Microscope/Lund, Philips C. BioTWIN Cryo. (2016).  
736 <http://www.polymat.lth.se/nchrem/microscopes/> (accessed January 5, 2016).
- 737 [17] N.B. Vargaftik, B.N. Volkov, L.D. Voljak, International Tables of the Surface Tension of  
738 Water, *J. Phys. Chem. Ref. Data.* 12 (1983) 817. doi:10.1063/1.555688.
- 739 [18] R. a. Campbell, H.P. Wacklin, I. Sutton, R. Cubitt, G. Fragneto, FIGARO: The new  
740 horizontal neutron reflectometer at the ILL, *Eur. Phys. J. Plus.* 126 (2011) 107.  
741 doi:10.1140/epjp/i2011-11107-8.
- 742 [19] J.R.P. Webster, S. Langridge, R.M. Dalglish, T.R. Charlton, Reflectometry techniques on  
743 the second target station at ISIS: Methods and science, *Eur. Phys. J. Plus.* 126 (2011) 1–5.  
744 doi:10.1140/epjp/i2011-11112-y.
- 745 [20] W. Stillwell, *An Introduction to Biological Membranes*, Elsevier, 2013. doi:10.1016/B978-0-  
746 444-52153-8.00011-8.
- 747 [21] A. Nelson, Co-refinement of multiple-contrast neutron/X-ray reflectivity data using  
748 MOTOFIT, *J. Appl. Crystallogr.* 39 (2006) 273–276. doi:10.1107/S0021889806005073.
- 749 [22] J. Sturtevant, Biochemical Applications Of Differential Scanning Calorimetry, *Annu. Rev.*  
750 *Phys. Chem.* 38 (1987) 463–488. doi:10.1146/annurev.physchem.38.1.463.
- 751 [23] G. Bruylants, J. Wouters, C. Michaux, Differential scanning calorimetry in life science:  
752 thermodynamics, stability, molecular recognition and application in drug design., *Curr. Med.*  
753 *Chem.* 12 (2005) 2011–2020. doi:10.2174/0929867054546564.
- 754 [24] E.R. Andrew, A. Bradbury, R.G. Eades, Nuclear Magnetic Resonance Spectra from a Crystal  
755 rotated at High Speed, *Nature.* 182 (1958) 1659–1659. doi:10.1038/1821659a0.
- 756 [25] A.E. Bennett, C.M. Rienstra, M. Auger, K. V Lakshmi, R.G. Griffin, Heteronuclear  
757 decoupling in rotating solids, *J. Chem. Phys.* 103 (1995) 6951–6958. doi:10.1063/1.470372.
- 758 [26] R.K. Harris, E.D. Becker, S.M. De Cabral Menezes, P. Granger, R.E. Hoffman, K.W. Zilm,  
759 Further Conventions for NMR shielding and chemical shifts (IUPAC recommendations  
760 2008), *Magn. Reson. Chem.* 46 (2008) 582–598. doi:10.1002/mrc.2225.
- 761 [27] A. Pines, M.G. Gibby, J.S. Waugh, Proton-enhanced nuclear induction spectroscopy <sup>13</sup>C  
762 chemical shielding anisotropy in some organic solids, *Chem. Phys. Lett.* 15 (1972) 373–376.  
763 doi:10.1016/0009-2614(72)80191-X.
- 764 [28] G. a. Morris, R. Freeman, Enhancement of Nuclear Magnetic Resonance Signals by  
765 Polarization Transfer, *J. Am. Chem. Soc.* 233 (1979) 760–762. doi:Doi  
766 10.1021/Ja00497a058.
- 767 [29] A.L. van Geet, Calibration of Methanol Nuclear Magnetic Resonance Thermometer at Low  
768 Temperature Simultaneous Spectrophotometric Determination of Hydrogen Peroxide and  
769 Peroxyacids of Sulfur, *Anal. Chem.* 42 (1970) 679–680. doi:10.1021/ac60288a022.
- 770 [30] L. Chen, Z. Weng, L. Goh, M. Garland, An efficient algorithm for automatic phase  
771 correction of NMR spectra based on entropy minimization, *J. Magn. Reson.* 158 (2002) 164–  
772 168. doi:10.1016/S1090-7807(02)00069-1.
- 773 [31] J.D. van Beek, matNMR: A flexible toolbox for processing, analyzing and visualizing  
774 magnetic resonance data in Matlab??, *J. Magn. Reson.* 187 (2007) 19–26.  
775 doi:10.1016/j.jmr.2007.03.017.

- 776 [32] A. Nowacka, P.C. Mohr, J. Norrman, R.W. Martin, D. Topgaard, Polarization transfer solid-  
777 state NMR for studying surfactant phase behavior, *Langmuir*. 26 (2010) 16848–16856.  
778 doi:10.1021/la102935t.
- 779 [33] A. Nowacka, N.A. Bongartz, O.H.S. Ollila, T. Nylander, D. Topgaard, Signal intensities in  
780 <sup>1</sup>H-<sup>13</sup>C CP and INEPT MAS NMR of liquid crystals, *J. Magn. Reson.* 230 (2013) 165–175.  
781 doi:10.1016/j.jmr.2013.02.016.
- 782 [34] A. Nowacka, S. Douezan, L. Wadsö, D. Topgaard, E. Sparr, Small polar molecules like  
783 glycerol and urea can preserve the fluidity of lipid bilayers under dry conditions, *Soft Matter*.  
784 8 (2012) 1482. doi:10.1039/c1sm06273e.
- 785 [35] Q.D. Pham, D. Topgaard, E. Sparr, Cyclic and Linear Monoterpenes in Phospholipid  
786 Membranes: Phase Behavior, Bilayer Structure, and Molecular Dynamics, *Langmuir*. 31  
787 (2015) 11067–11077. doi:10.1021/acs.langmuir.5b00856.
- 788 [36] W.L. Earl, D.L. VanderHart, Observations in Solid Polyethylenes by Carbon-13 Nuclear  
789 Magnetic Resonance with Magic Angle Sample Spinning, *Macromolecules*. 12 (1979) 762–  
790 767. doi:10.1021/ma60070a045.
- 791 [37] J. Seelig, A. Seelig, Lipid conformation in model membranes and biological membranes., *Q.*  
792 *Rev. Biophys.* 13 (1980) 19–61. doi:10.1017/S0033583500000305.
- 793 [38] D. Vaknin, K. Kjaer, J. Als-Nielsen, M. Lösche, Structural properties of phosphatidylcholine  
794 in a monolayer at the air/water interface, *Biophys. J.* 59 (1991) 1325–1332.  
795 doi:10.1016/S0006-3495(91)82347-5.
- 796 [39] A.P. Dabkowska, L.E. Collins, D.J. Barlow, R. Barker, S.E. Mclain, M.J. Lawrence, et al.,  
797 Modulation of dipalmitoylphosphatidylcholine monolayers by dimethyl sulfoxide, *Langmuir*.  
798 30 (2014) 8803–8811. doi:10.1021/la501275h.
- 799 [40] R.M. Moebius, *Novel Methods to Study Interfacial Layers*, 1st Editio, Elsevier Science,  
800 2001.
- 801 [41] M.K. and S.I.C. Nils O Petersen, Paulus A Kroon, Thermal phase transitions in deuterated  
802 lecithin bilayers, *Chem. Physicss Lipids* 14. 14 (1975) 343–349.
- 803 [42] J. Ulander, A.D.J. Haymet, Permeation across hydrated DPPC lipid bilayers: simulation of  
804 the titrable amphiphilic drug valproic acid., *Biophys. J.* 85 (2003) 3475–3484.  
805 doi:10.1016/S0006-3495(03)74768-7.
- 806 [43] A. Nelson, Co-refinement of multiple-contrast neutron/X-ray reflectivity data using  
807 MOTOFIT, *J. Appl. Crystallogr.* 39 (2006) 273–276. doi:10.1107/S0021889806005073.
- 808 [44] T. Mavromoustakos, E. Theodoropoulou, D.P. Yang, The use of high-resolution solid-state  
809 NMR spectroscopy and differential scanning calorimetry to study interactions of anaesthetic  
810 steroids with membrane, *Bba.Biomembranes*. 1328 (1997) 65–73.
- 811 [45] J.-X. Cheng, S. Pautot, D.A. Weitz, X.S. Xie, Ordering of water molecules between  
812 phospholipid bilayers visualized by coherent anti-Stokes Raman scattering microscopy.,  
813 *Proc. Natl. Acad. Sci. U. S. A.* 100 (2003) 9826–9830. doi:10.1073/pnas.1732202100.
- 814 [46] Y. a Domanov, P.K.J. Kinnunen, Antimicrobial peptides temporins B and L induce  
815 formation of tubular lipid protrusions from supported phospholipid bilayers., *Biophys. J.* 91  
816 (2006) 4427–4439. doi:10.1529/biophysj.106.091702.

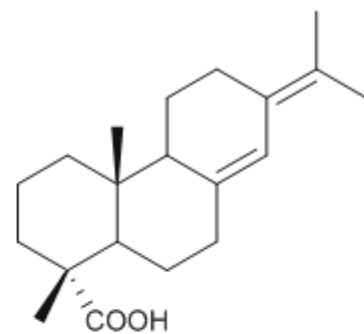
- 817 [47] L.D. Renner, D.B. Weibel, Cardiolipin microdomains localize to negatively curved regions  
818 of *Escherichia coli* membranes., *Proc. Natl. Acad. Sci. U. S. A.* 108 (2011) 6264–6269.  
819 doi:10.1073/pnas.1015757108.
- 820 [48] R. Waninge, T. Nylander, M. Paulsson, B. Bergenståhl, Milk membrane lipid vesicle  
821 structures studied with Cryo-TEM, *Colloids Surfaces B Biointerfaces.* 31 (2003) 257–264.  
822 doi:10.1016/S0927-7765(03)00145-0.
- 823 [49] A. Åkesson, T. Lind, N. Ehrlich, D. Stamou, H. Wacklin, M. Cárdenas, Composition and  
824 structure of mixed phospholipid supported bilayers formed by POPC and DPPC, *Soft Matter.*  
825 8 (2012) 5658. doi:10.1039/c2sm00013j.
- 826 [50] J. Larsen, N.S. Hatzakis, D. Stamou, Observation of inhomogeneity in the lipid composition  
827 of individual nanoscale liposomes, *J. Am. Chem. Soc.* 133 (2011) 10685–10687.  
828 doi:10.1021/ja203984j.
- 829 [51] A. Cruz, L. Vázquez, M. Vélez, J. Pérez-Gil, Effect of pulmonary surfactant protein SP-B on  
830 the micro- and nanostructure of phospholipid films., *Biophys. J.* 86 (2004) 308–320.  
831 doi:10.1016/S0006-3495(04)74106-5.
- 832 [52] J.V.N. Ferreira, T.M. Capello, L.J.A. Siqueira, J.H.G. Lago, L. Caseli, Mechanism of Action  
833 of Thymol on Cell Membranes Investigated through Lipid Langmuir Monolayers at the Air–  
834 Water Interface and Molecular Simulation, *Langmuir.* 32 (2016) 3234–3241.  
835 doi:10.1021/acs.langmuir.6b00600.
- 836 [53] H.S. Camargos, R.A. Moreira, S.A. Mendanha, K.S. Fernandes, M.L. Dorta, A. Alonso,  
837 Terpenes increase the lipid dynamics in the *Leishmania* plasma membrane at concentrations  
838 similar to their IC<sub>50</sub> values, *PLoS One.* 9 (2014). doi:10.1371/journal.pone.0104429.
- 839 [54] G. Peng, J.C. Roberts, Solubility and toxicity of resin acids, *Water Res.* 34 (2000) 2779–  
840 2785. doi:10.1016/S0043-1354(99)00406-6.
- 841 [55] J.N. Israelachvili, D.J. Mitchell, B.W. Ninham, Theory of self-assembly of hydrocarbon  
842 amphiphiles into micelles and bilayers, *J. Chem. Soc. Faraday Trans. 2.* 72 (1976) 1525.  
843 doi:10.1039/f29767201525.
- 844 [56] T.J. McIntosh, Differences in hydrocarbon chain tilt between hydrated  
845 phosphatidylethanolamine and phosphatidylcholine bilayers. A molecular packing model,  
846 *Biophys. J.* 29 (1980) 237–245. doi:10.1016/S0006-3495(80)85128-9.
- 847 [57] C.L. Yaws, *Yaws' Handbook of Thermodynamic and Physical Properties of Chemical*  
848 *Compounds*, Knovel, 2003. <http://app.knovel.com/web/toc.v/cid:kpYHTPPCC4/> (accessed  
849 December 10, 2015).
- 850 [58] T.M. Krygowski, Crystallographic studies of inter- and intramolecular interactions reflected  
851 in aromatic character of Pi-electron systems, *J. Chem. Inf. Model.* 33 (1993) 70–78.  
852 doi:10.1021/ci00011a011.
- 853
- 854



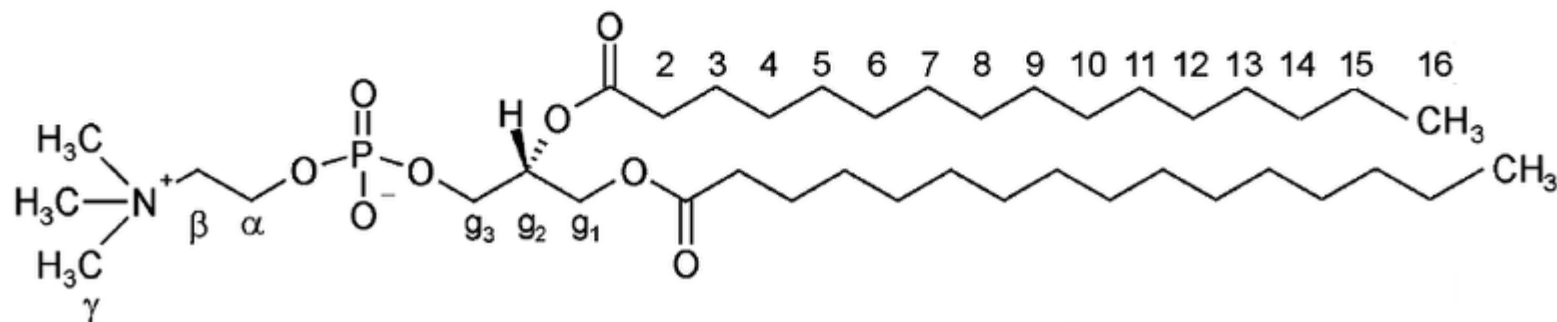
Dichlorodehydroabietic acid



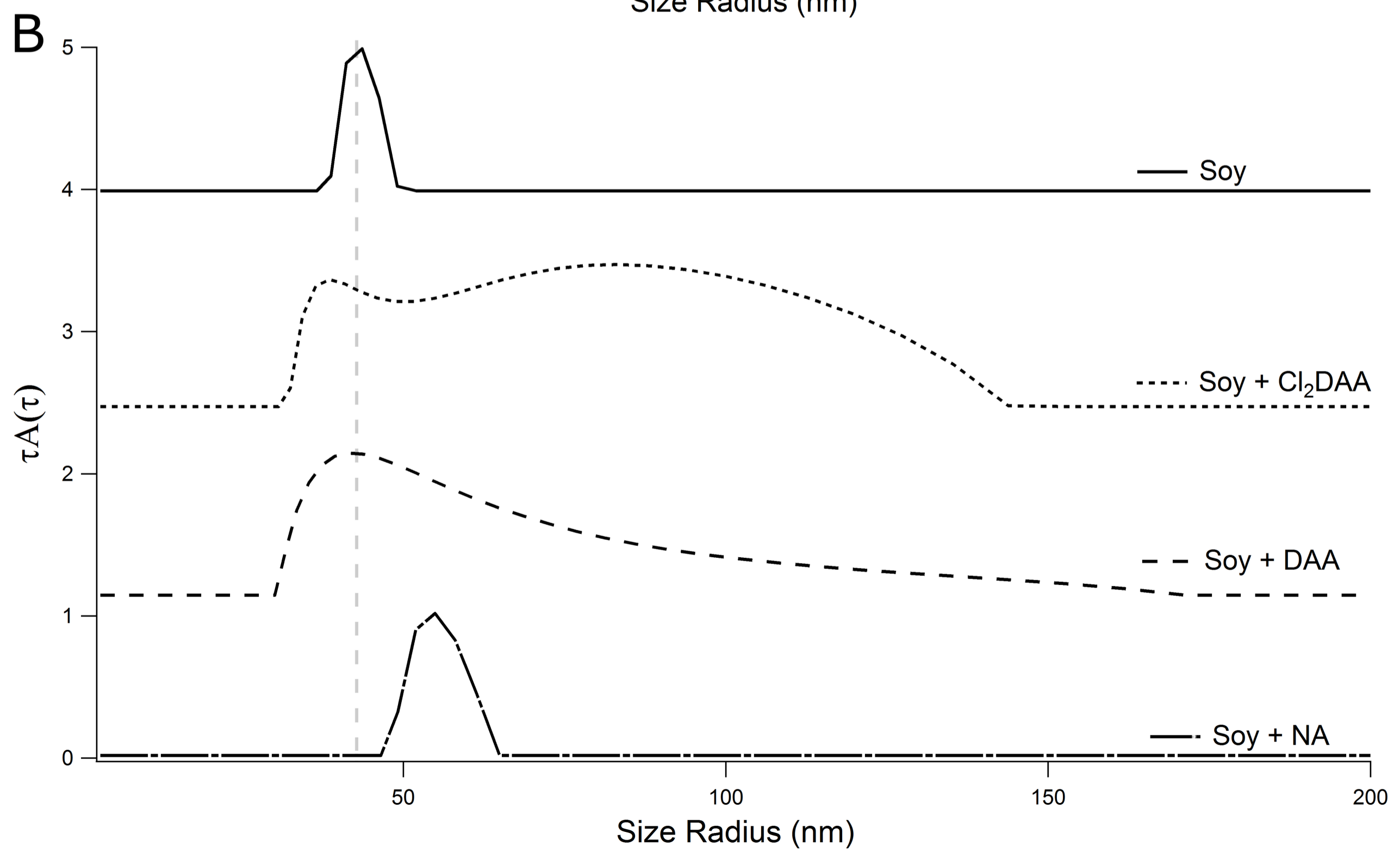
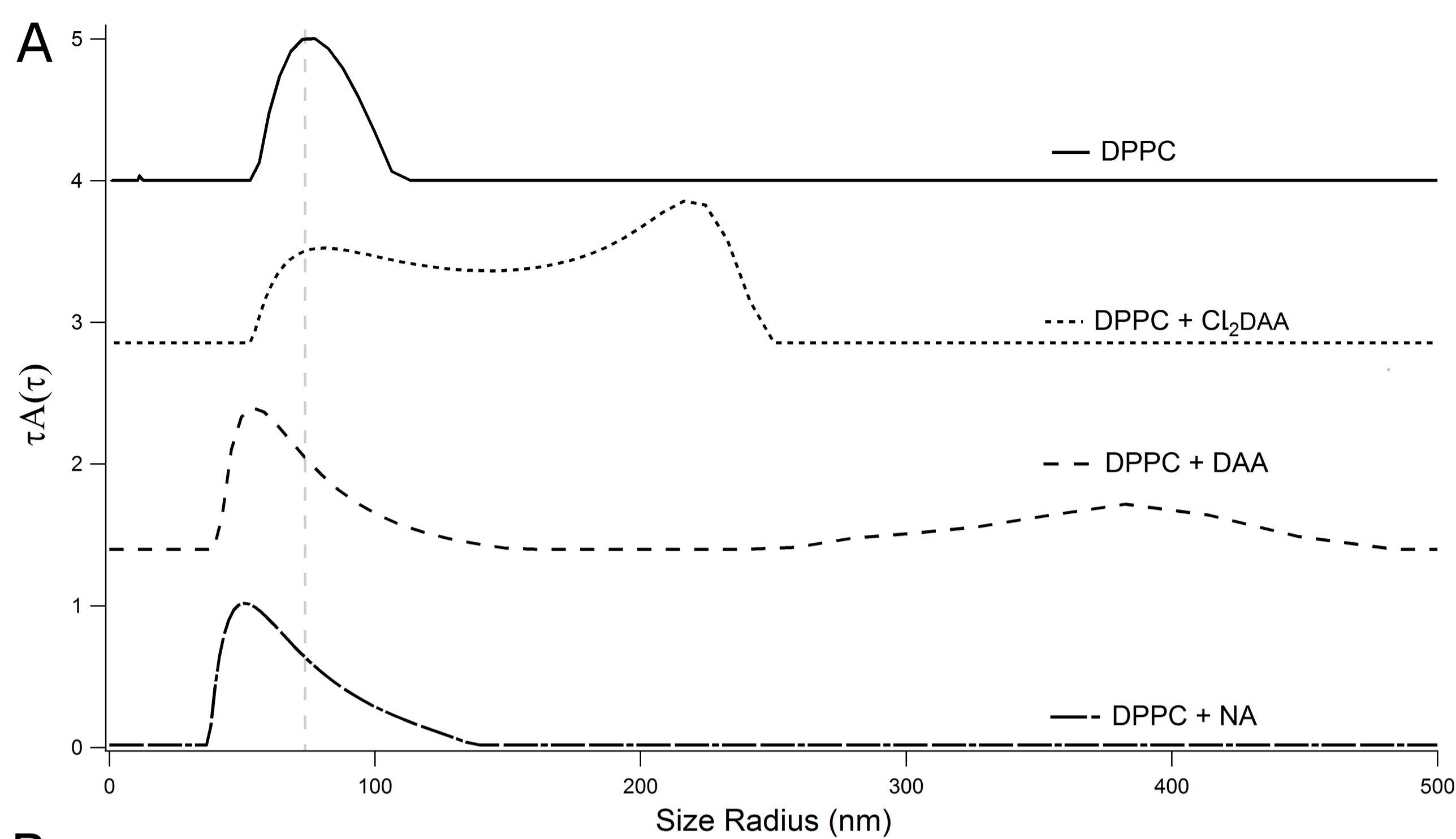
Dehydroabietic acid

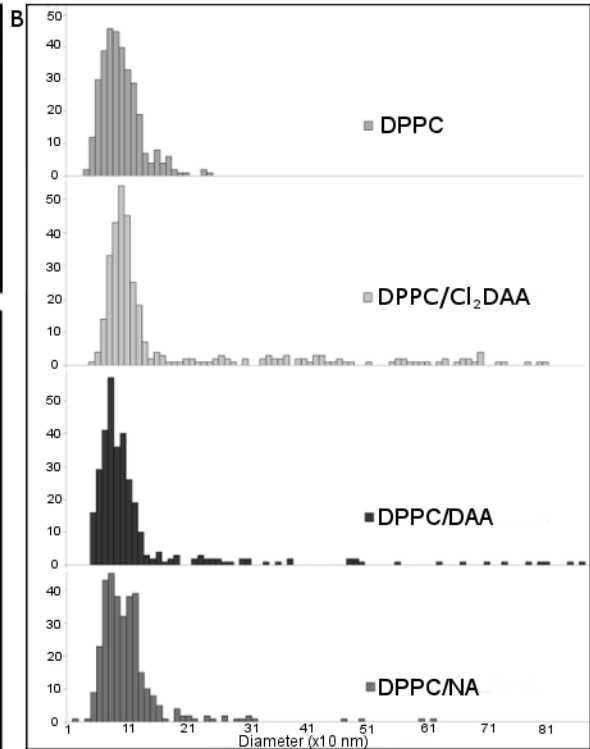
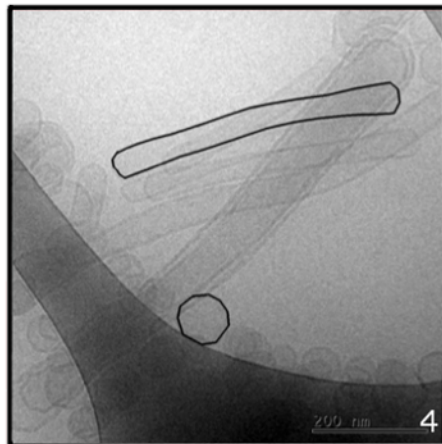
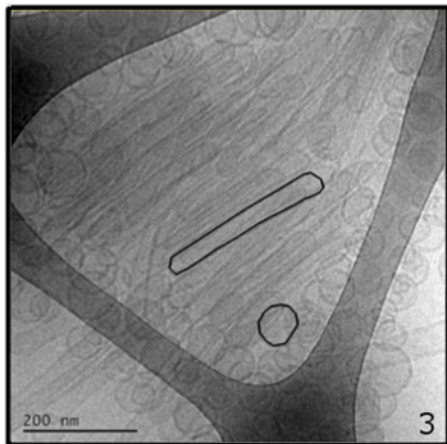
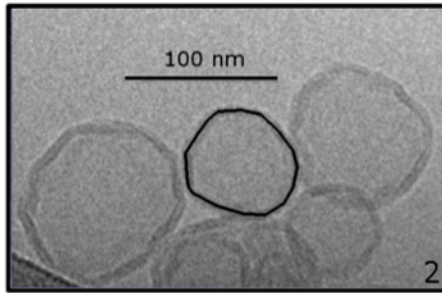
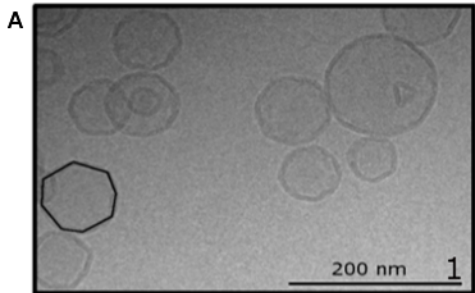


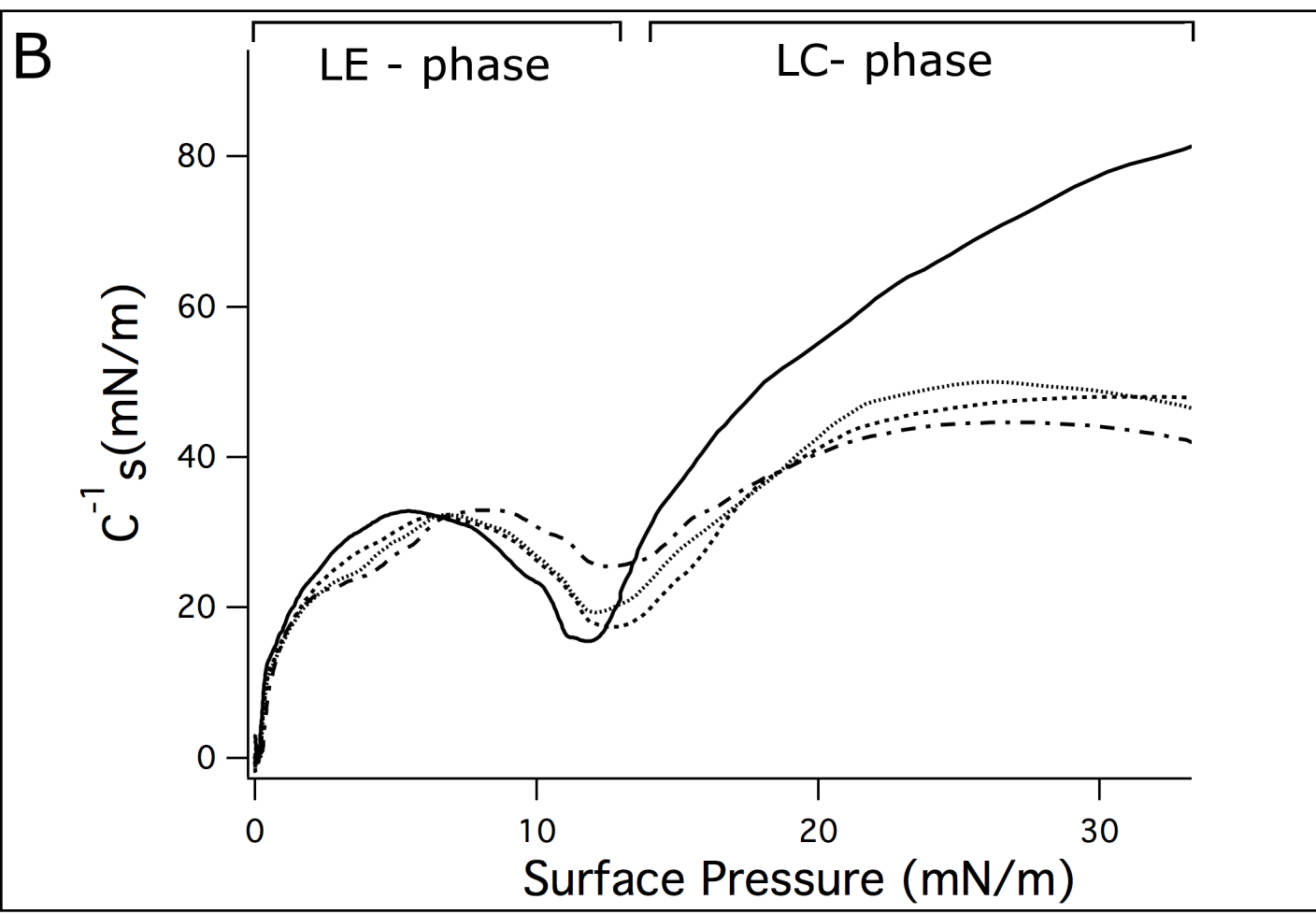
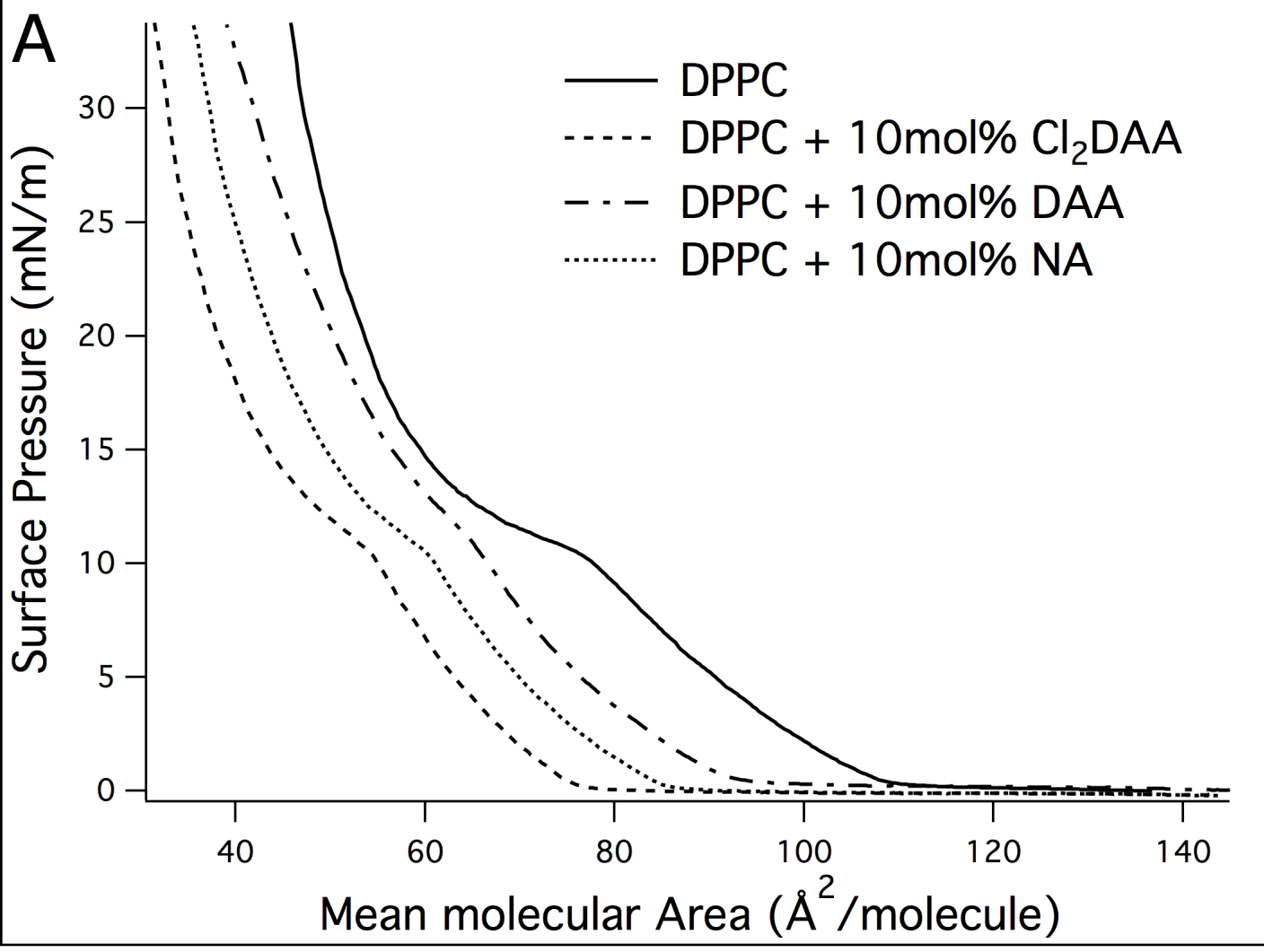
Neoabietic acid

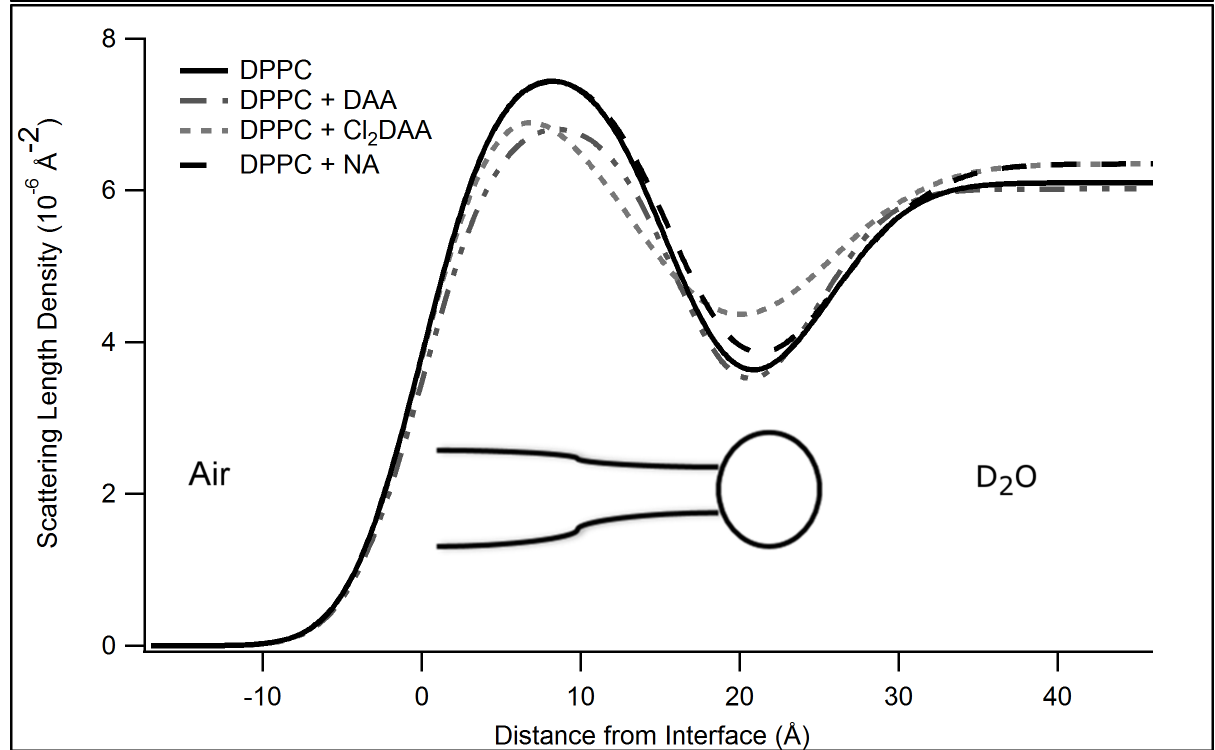
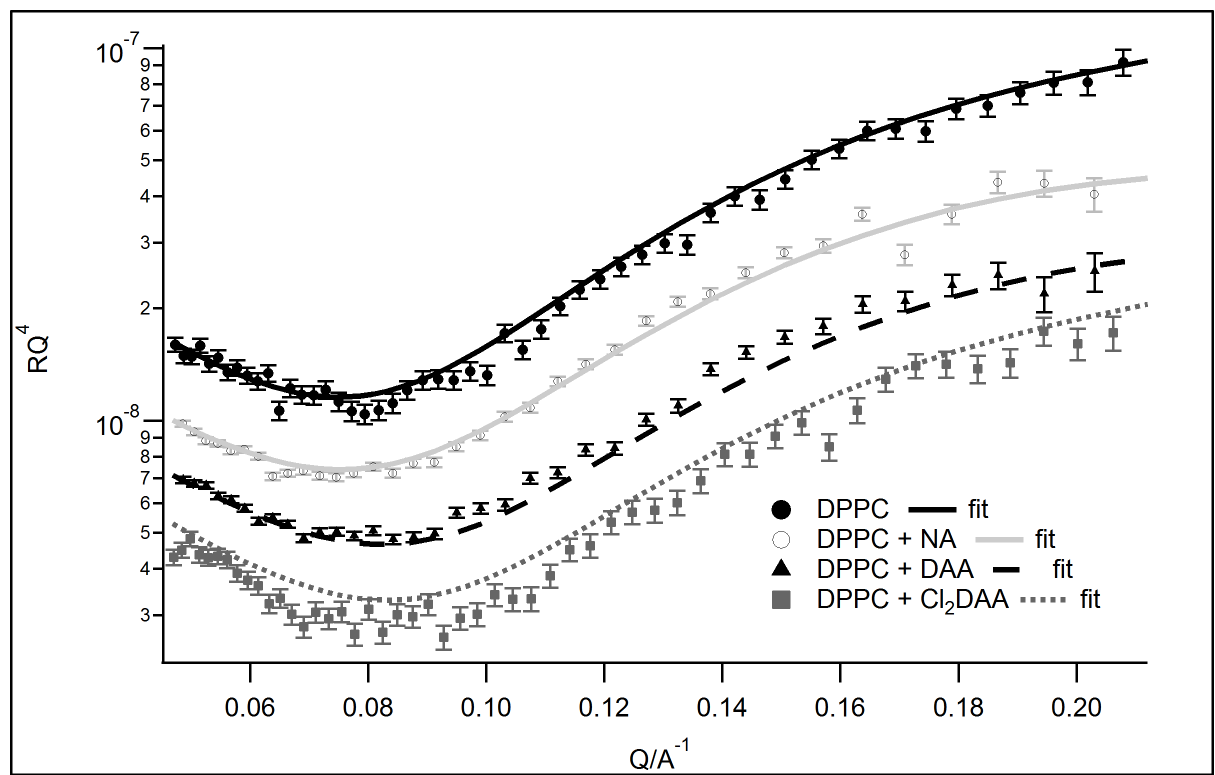


Dipalmitoylphosphatidylcholine



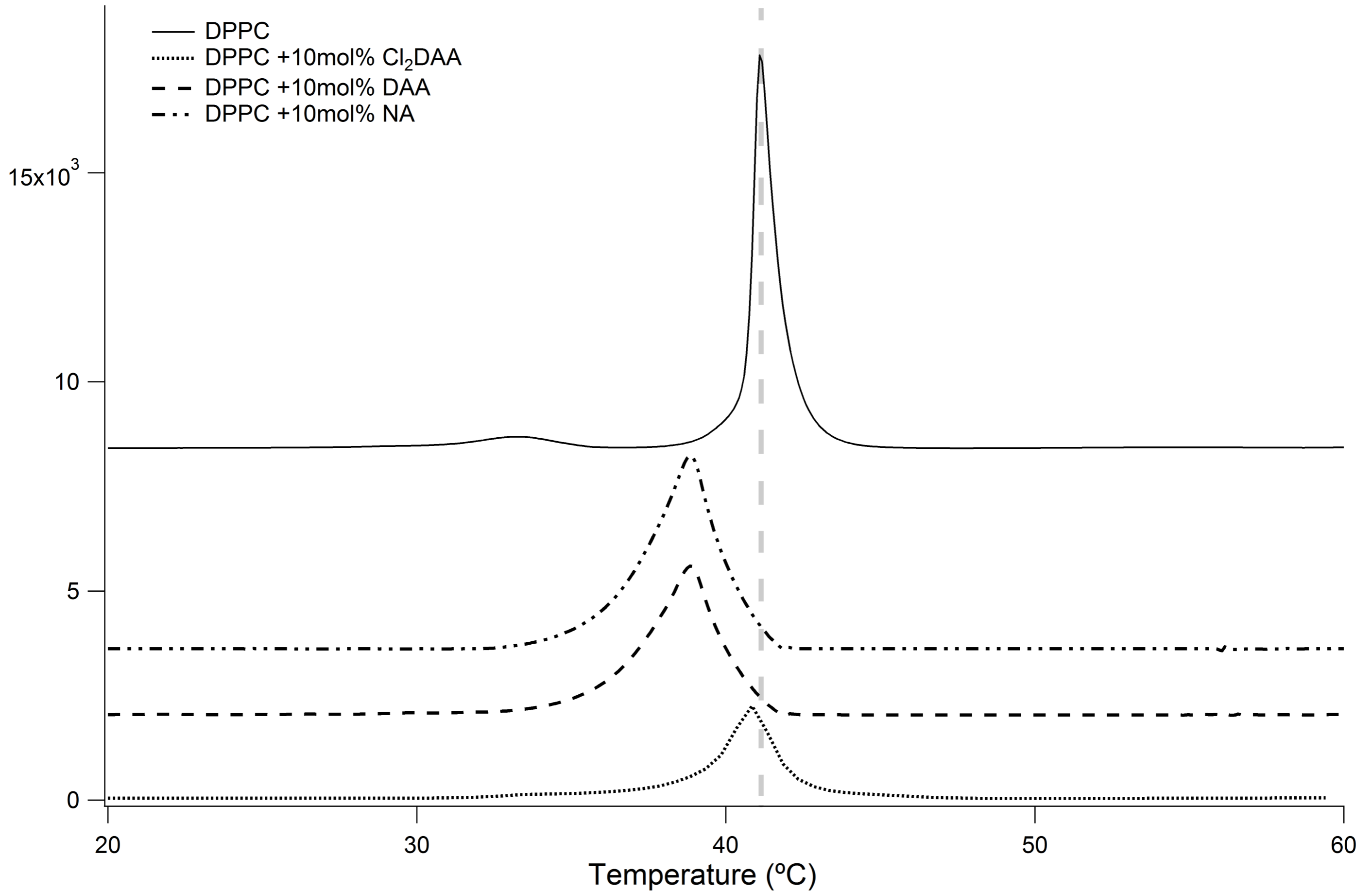


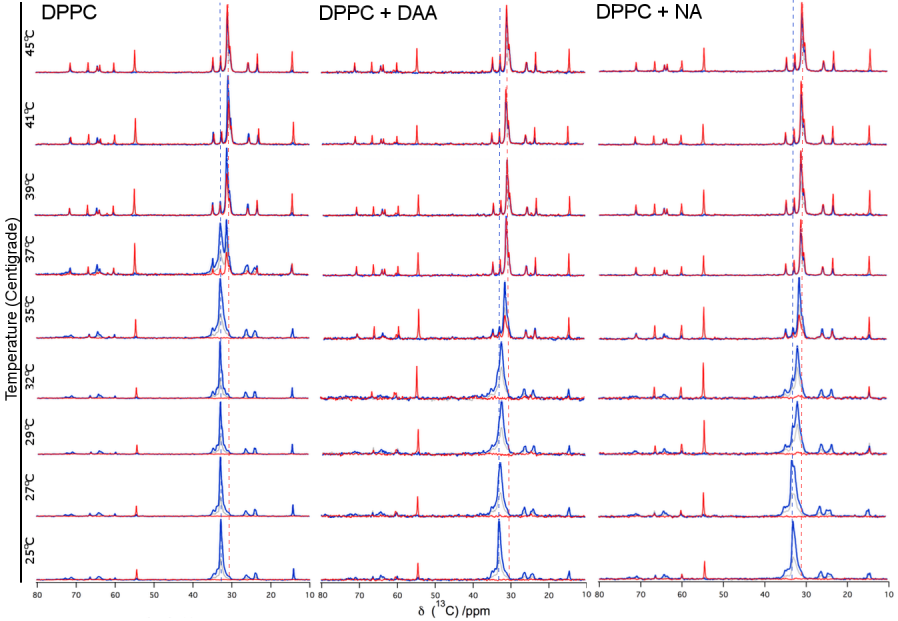


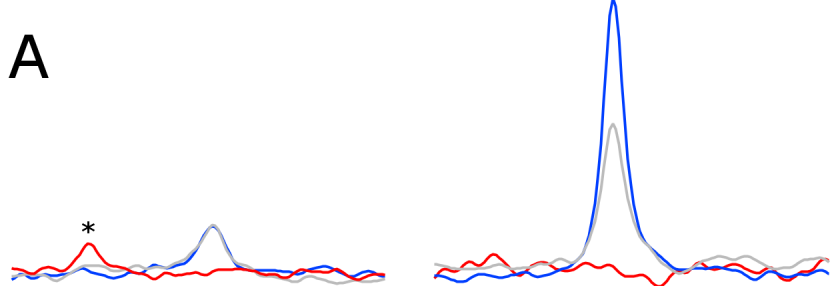
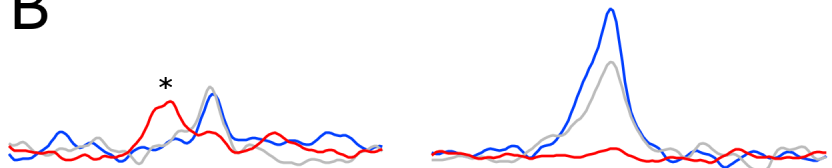
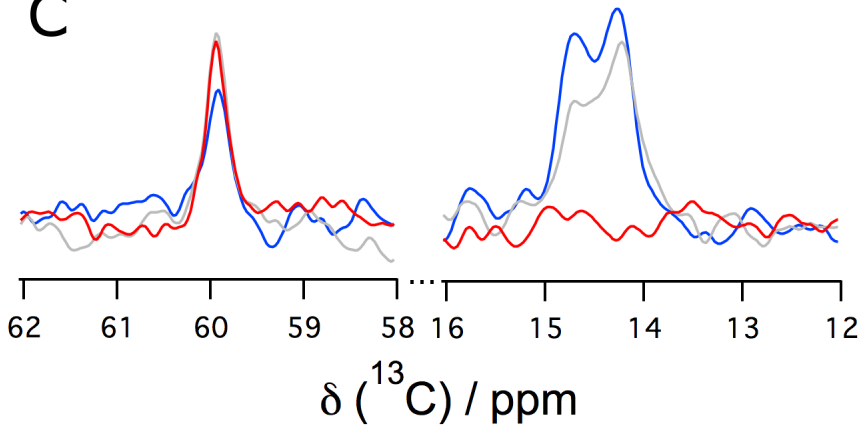




enthalpy (cal/mole/°C)

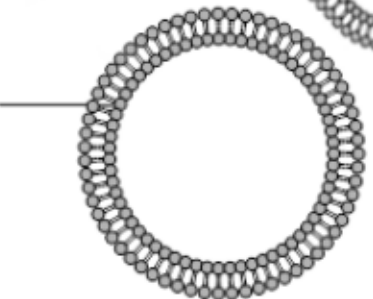
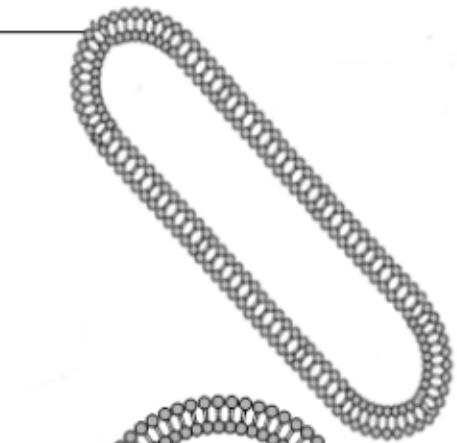
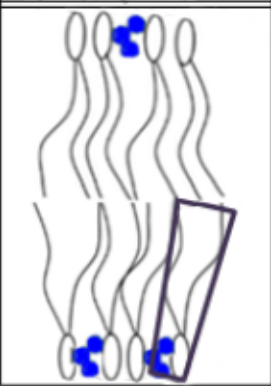
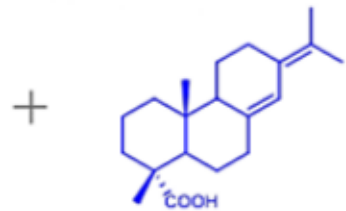
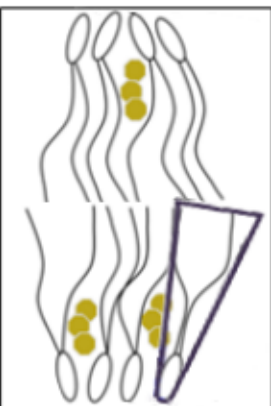
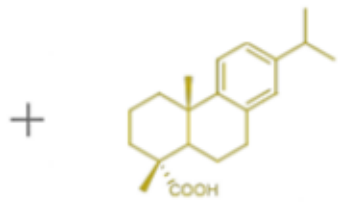




**A****B****C**



DPPC



	Tail Layer thickness (Å)	Head group Layer thickness (Å)	Roughness head/tail interface	Solvent penetration (%) head group
<b>DPPC</b>	16.2 ± 0.2	8.9 ± 0.5	3.7 ± 0.2	15 ± 5
<b>DPPC/Cl<sub>2</sub>DAA</b>	14.7 ± 0.1	8.5 ± 0.3	6.0 ± 0.2	6 ± 4
<b>DPPC/DAA</b>	16.4 ± 0.1	7.6 ± 0.2	3.7 ± 0.2	9 ± 2
<b>DPPC/NA</b>	15.6 ± 0.1	9.4 ± 0.5	4.4 ± 0.1	21 ± 5

Mixture	$\Delta H$ (kcal/mol)	$\Delta H_{vH}$ (kcal/mol)	CU	T <sub>m</sub>
<b>DPPC</b>	12 ± 1.0	541.2 ± 0.4	44 ± 5	41 ± 1
<b>+ 5 mol% Cl<sub>2</sub>DAA</b>	13.1 ± 0.7	364 ± 1.2	27 ± 3	41 ± 1
<b>+ 10 mol% Cl<sub>2</sub>DAA</b>	5.8 ± 0.5	300.0 ± 0.3	52 ± 6	40 ± 1
<b>+ 10 mol% DAA</b>	14 ± 2.0	241.0 ± 0.3	16 ± 3	38 ± 1
<b>+ 10 mol% NA</b>	18 ± 1.0	213.2 ± 0.1	12 ± 1	38 ± 1